

Chen H, Liang Q, Liu Y, Xie S.

[Hydraulic correction method \(HCM\) to enhance the efficiency of SRTM DEM  
in flood modeling.](#)

*Journal of Hydrology* 2018, 559, 56-70.

**Copyright:**

© 2018. This manuscript version is made available under the [CC-BY-NC-ND 4.0 license](#)

**DOI link to article:**

<https://doi.org/10.1016/j.jhydrol.2018.01.056>

**Date deposited:**

06/03/2018

**Embargo release date:**

10 February 2019



This work is licensed under a  
[Creative Commons Attribution-NonCommercial-NoDerivatives 4.0 International licence](#)

# **Hydraulic Correction Method (HCM) to Enhance the Efficiency of SRTM DEM in Flood Modeling**

Huili Chen<sup>1, 2</sup>, Qiuhua Liang<sup>3</sup>, Yong Liu<sup>1\*</sup>, Shuguang Xie<sup>1</sup>

1. College of Environmental Science and Engineering, Key Laboratory of Water and Sediment Sciences (MOE), Peking University, Beijing 100871, China.
2. Laboratory for Earth Surface Processes, Ministry of Education, Peking University, Beijing 100871, China
3. School of Engineering, Newcastle University, UK

\* Corresponding Author:

E-mail: yongliu@pku.edu.cn (Y. Liu); TEL: 86 10 62753184; FAX: 86 10 62754180.

## 1    **ABSTRACT**

2    Digital Elevation Model (DEM) is one of the most important controlling factors determining  
3    the simulation accuracy of hydraulic models. However, the currently available global  
4    topographic data is confronted with limitations for application in 2-D hydraulic modeling,  
5    mainly due to the existence of vegetation bias, random errors and insufficient spatial resolution.  
6    A hydraulic correction method (HCM) for the SRTM DEM is proposed in this study to improve  
7    modeling accuracy. Firstly, we employ the global vegetation corrected DEM (i.e. Bare-Earth  
8    DEM), developed from the SRTM DEM to include both vegetation height and SRTM  
9    vegetation signal. Then, a newly released DEM, removing both vegetation bias and random  
10   errors (i.e. Multi-Error Removed DEM), is employed to overcome the limitation of height errors.  
11   Last, an approach to correct the Multi-Error Removed DEM is presented to account for the  
12   insufficiency of spatial resolution, ensuring flow connectivity of the river networks. The  
13   approach involves: (a) extracting river networks from the Multi-Error Removed DEM using an  
14   automated algorithm in ArcGIS; (b) correcting the location and layout of extracted streams with  
15   the aid of Google Earth platform and Remote Sensing imagery; and (c) removing the positive  
16   biases of the raised segment in the river networks based on bed slope to generate the  
17   hydraulically corrected DEM. The proposed HCM utilizes easily available data and tools to  
18   improve the flow connectivity of river networks without manual adjustment. To demonstrate  
19   the advantages of HCM, an extreme flood event in Huifa River Basin (China) is simulated on  
20   the original DEM, Bare-Earth DEM, Multi-Error removed DEM, and hydraulically corrected  
21   DEM using an integrated hydrologic-hydraulic model. A comparative analysis is subsequently  
22   performed to assess the simulation accuracy and performance of four different DEMs and

23 favorable results have been obtained on the corrected DEM.

24 **KEYWORDS:** DEM Correction; Vegetation Bias; Flow Connectivity; Two-dimensional

25 Hydraulic Model; SRTM

## 1 INTRODUCTION

The frequent occurrence of extreme floods (e.g., Pakistan in 2010; Thailand in 2011; India in 2014; China in 2016) has drawn continuous attention from the public and research communities in recent years. Historically, flooding has been recognized as one of the main types of natural hazards in terms of economic damages and casualties (Dottori et al., 2016). Between 1980 and 2013, flooding had caused about \$1 trillion direct economic losses and 220,000 fatalities (Re, 2014). Flood induced damages and casualties are widely predicted to dramatically increase due to economic development and population growth (Winsemius et al., 2015), land use/cover change (Saghafian et al., 2008; Ward et al., 2008) and climate change (Alexander et al., 2006; Lu et al., 2016; Quintana-Seguí et al., 2016; Cheng et al., 2017a; Cheng et al., 2017b). Implementing more effective flood risk reduction and management strategies has become an important task for governments at different levels across the world.

In recent years, significant efforts have been made to better understand the physical process of flooding and develop different types of models to predict flood hazard. Numerical/mathematical models for quantifying and mapping flood hazards and risks have become effective tools in facilitating flood risk management and reducing the catastrophic impacts (European Commission, 2007). Many up-to-date advanced hydro-system analysis methods, e.g. discrete principal-monotonicity method (Cheng et al., 2006a; Cheng et al., 2006b), have been developed to simulate highly complicated hydrological processes, which are based on the responses between input and output datasets. Besides the data-driven models, mechanism-based flood models have also been developed with different levels of complexity, ranging from the simplified lumped approaches, distributed hydrological models, to the highly

detailed 2-D hydraulic models. The data-driven models and lumped models (e.g. GR model, Perrin et al., 2003) deal with the system as a whole and do not consider the spatial heterogeneity of the problem domain (Khakbaz et al., 2012). However, flooding may present clear spatial variations as influenced by localized weather and topographic conditions (Chen et al., 2017a; Cheng et al., 2017c; Cheng et al., 2017d). Distributed hydrological models (e.g. SWAT, Arnold et al., 1998) take into account the heterogeneities in both the catchment characteristics and hydrometeorological inputs (Nguyen et al., 2015; Chen et al., 2017b). However, they usually adopt conceptual or simplified approaches to route runoffs and flood waves (Khan & Valeo, 2016), and are incapable of representing certain common flow phenomena, such as flow over flat slopes, reversing flow, and backwater effect (Kim et al., 2012). This may constrain the wider application in flood risk management where detailed floodplain hydrodynamics is typically required. The 2-D hydraulic models can simulate the dynamics of surface runoff across watersheds with complex topographies using minimal model parameters, in accordance with continuity and momentum principles. Hydraulic models better depict the dynamics of flood waves and physical characteristics of the watersheds. With the availability of rich sources of high-resolution topographic and hydrological data and much enhanced computational power, a number of 2-D hydraulic models have been successfully applied to flood simulations at the watershed scale (e.g. Neal et. al., 2012; Paiva et. al., 2013).

Hydraulic models rely on accurate topographic data to reliably predict flooding processes over landscapes (Callow et al., 2007). The accuracy of DEM has been viewed as the most important controlling factor determining the simulation accuracy of hydraulic models (Bates et al., 1998; Sanders, 2007; Jarihani et al., 2015). To date, the Shuttle Radar Topographic Mission (SRTM)

Digital Elevation Model (DEM) ([Rabus et al., 2003](#); [Farr et al., 2007](#)) is thought to be the most popular and best freely available topographic data that covers most parts of the globe surface ([Hirt et al., 2010](#); [Jing et al., 2014](#); [Athmania & Achour, 2014](#); [Sampson et al., 2015](#)). An alternative to SRTM is ASTER (the Advanced Spaceborne Thermal Emission and Reflection Radiometer, [Fujisada et al., 2012](#)). However, although the spatial resolution of ASTER (30 m) has an advantage over that of SRTM (90 m), SRTM is more suitable for hydraulic modeling as it is distorted by fewer surface objects with higher vertical accuracy ([Jing et al., 2014](#); [Athmania & Achour, 2014](#); [Varga & Bašić, 2015](#); [Chaieb et al., 2016](#)). For these reasons, this study will focus on SRTM DEM.

SRTM DEM has been widely used for flood modeling in previous studies (e.g. [Sanders, 2007](#); [Samantaray et al., 2015](#); [Fernández et al., 2016](#)). But, all of the existing works have faced the same challenge, i.e. how to remove the vegetation bias presented in the original SRTM DEM and to obtain a Bare-Earth DEM from SRTM DEM ([O'Loughlin et al., 2016](#)). The inability of the C-band radar employed by SRTM to completely penetrate the vegetation canopy to the ground has caused significant positive biases in the SRTM DEM ([Brown et al., 2010](#)). Thus, the original SRTM DEM may overestimate the ground elevation in certain areas ([Carabajal & Harding, 2005](#); [Lalonde et al., 2010](#); [Shortridge & Messina, 2011](#); [Wang et al., 2012](#)). [Baugh et al. \(2013\)](#) indicated that removing the vegetation bias for SRTM DEM in a reach of the Amazon Basin clearly improved hydrodynamic modeling accuracy in terms of both water depth and inundation extent. A number of other researchers have also tried to correct the vegetation bias before flood modeling. However, all of these existing works did not consider either the spatial variability of the vegetation height ([Wilson et al., 2007](#); [Coe et al., 2008](#); [Paiva et al.,](#)

2011) or the spatial variability of SRTM vegetation permeation signal (Baugh et al., 2013; Pinel et al., 2015; Luo et al., 2017). Besides, all of the studies mentioned above have conducted in the Amazon Basin. So more case studies with different watershed characteristics should be further considered to better understand the problem. Recently, the release of global forest canopy heights (Lefsky, 2010; Simard et al., 2011) and other related remote sensing products has provided a desirable opportunity to enable systematic vegetation corrections for SRTM DEM, accounting for the spatial variability of both vegetation height and SRTM vegetation signal. O'Loughlin et al. (2016) combined these remote sensing datasets to correct the vegetation bias in the original SRTM DEM and developed the first global Bare-Earth DEM. The Bare-Earth DEM showed great improvements in vertical accuracy of the vegetated areas and is openly available. In this study, we will first attempt to examine this utility of the Bare-Earth DEM for flood inundation modeling in a natural basin outside of the Amazon Basin.

In addition to the vegetation bias, SRTM DEM also contains various random errors, which are non-negligible for flood modeling. Random errors can be classified by their spatial scale into speckle noise, strip noise and absolute bias (Yamazaki et al., 2017). The presence of speckle noise is one common characteristic of SAR DEMs like SRTM (Zandbergen, 2008), mainly caused by variability of surface reflectance over flat terrain (Takaku et al., 2016). Speckle noise has the consequence of increasing slope estimates at short distances (Alsdorf et al. 2007; Falorni et al. 2005; Kielet al. 2006). Speckling generally has a negative effect on flood modeling, in particular, in areas of floodplain with low slopes. Stripe noise is a regular height undulation with a wavelength of 500 m to 100 km (Gallant and Read, 2009; Tarekegn and Sayama, 2013; Yamazaki et al., 2017). The stripe noise of the SRTM DEM is mainly caused by uncompensated



114 mast motion error ([Walker et al., 2007](#)), which can cause significant errors in simulating spatial  
115 flood extent ([Tarekegn and Sayama, 2013](#)). The absolute bias can be regarded as a departure in  
116 the average elevation over a large domain (typically >20 km scale) ([Yamazaki et al., 2017](#)),  
117 caused by long-wavelength random residual satellite motion errors ([Rodriguez et al., 2006](#)).  
118 The spatial pattern of absolute bias is not homogeneous because multiple data with different  
119 absolute biases were overlaid during the creation procedure of SRTM DEM. Thus it is highly  
120 necessary to eliminate multiple error components (including vegetation bias and three random  
121 errors) before integrating the SRTM DEM in flood modeling. However, treating multiple error  
122 components is not easy, because different error components could offset each other and thus  
123 difficult to accurately recognize and estimate error magnitude. Fortunately, [Yamazaki et al.](#)  
124 [\(2017\)](#) newly released the first global “Multi-Error-Removed Improved-Terrain DEM” by  
125 correcting all major error components in SRTM DEM, which shows better vertical accuracy  
126 than the original DEM. In this study, we will simultaneously examine this utility of the Bare-  
127 Earth DEM and Multi-Error Removed DEM for flood inundation modeling.

128 Besides the multiple height errors, the spatial resolution of global SRTM DEM (90 m) are not  
129 fine enough to represent the small-scale topographic features such as narrow river or channel  
130 networks. They are the key elements for reliable depiction of watershed hydrodynamics in  
131 hydraulic models, especially for the watersheds with complex terrain ([Yamazaki et al., 2012](#);  
132 [Schumann et al., 2014](#)). Moreover, SRTM is influenced by surface artifacts such as artificial  
133 buildings, which may break flow connectivity along channel networks or between the river  
134 channel and hillslope systems ([Callow et al. 2007](#); [Sanders, 2007](#); [Lehner et al., 2008](#)). Thus,  
135 the DEM needs to be pre-processed to better represent hydrological characteristics, particularly

in places where the flow connectivity is lost.

Various algorithms have been developed for hydrologically correcting DEMs. It is usually considered that one of the major challenges impeding flow connectivity is the “pit(s)”, i.e. one or more adjacent pixels with lower elevation values than its or their surrounded pixels. The “pit(s)” can unphysically block water and cause disconnected flow paths (Kenny et al., 2008; Lee et al., 2017). The common pit removal methods include lifting (Jenson & Domingue, 1988), carving (Martz & Garbrecht, 1999), and the combination of lifting and carving (Soille, 2004). These pits removal algorithms are useful for improving flow connectivity in DEMs with high spatial resolution, such as airborne LiDAR DEMs. However, they are not effective for the SRTM DEM because the elevation values of sub-pixel scale hydrology features may be also lifted by surrounding objects, such as bridge and building, etc. (Yamazaki et al., 2012). In the aforementioned algorithms, these pits are treated equally without considering whether they are “real” or spurious. Thus the “corrected” DEMs may not well represent the realistic terrains. Other related pre-processing methods include stream burning (e.g. Lehner et al., 2008) and ridge fencing (e.g. Masutomi et al., 2009), etc. But they also suffer from the same issue and create “corrected” DEMs that may not represent the realistic terrains. Yamazaki et al. (2012) proposed an alternative method that treated the river networks from the HydroSHEDS datasets (Lehner et al., 2008) as given information, and then removed the pits of the river networks to ensure flow connectivity along the rivers. Lehner et al. (2008) developed the river network dataset using mainly standard GIS techniques. The process of deriving river networks through pit filling is automated and simple in ESRI's ArcGIS software, but it cannot ensure the DEM-derived river networks resembling the known networks (Kenny et al., 2008), especially in those

flat areas (Pan et al., 2012). Moreover, when removing the pits in the river networks, the parameters of the adopted weighting function for deciding the level of modification were obtained by trial and error and needed manual adjustment; and they did not account for the terrain harmony between the networks and hillslopes.

To overcome the shortcomings of the existing DEM-correction methods for application of SRTM DEM in flood modeling, there is thereby a need to develop an approach to generate new hydraulically corrected DEM to support 2-D hydraulic simulation. On the basis of Multi-Error Removed DEM (Yamazaki et al. 2017), we proposed a new Hydraulic Correction Method (HCM) to effectively correct the DEM and ensure flow connectivity along the river/channel networks. Meanwhile, the vegetation bias will be investigated using the Bare-Earth DEM developed from SRTM DEM by O'Loughlin et al. (2016), accounting for the spatial variability of both vegetation height and SRTM vegetation signal. The Multi-Error Removed DEM is also investigated to test its utility in flood inundation simulation. The purpose of the current study is to identify the limitations of SRTM DEM in 2-D watershed hydraulic simulation, and to improve its utility based on available auxiliary data and tools.

## **2 METHODOLOGY**

### **2.1 New Hydraulic Correction Method (HCM) for the SRTM DEM**

In order to correct the SRTM DEM to better replicate the hydrology features of a watershed and improve hydraulic flood simulation results, the new Hydraulic Correction Method (HCM) is proposed as a) removing the vegetation bias and random errors; and b) ensuring flow connectivity (Figure 1). The Bare-Earth DEM developed is employed to account for the

vegetation bias in the SRTM DEM. The Multi-Error Removed DEM (Yamazaki et al. 2017) is adopted to investigate both the vegetation bias and random errors. In this sub-section, the approach to ensuring flow connectivity is introduced in detail.

### **2.1.1 Generation of River Networks**

Analysis algorithms have become widely available to extract river networks from DEMs. River networks are routinely defined as pixels with drainage areas that are greater than a threshold value. In this study, the preliminary networks are automatically generated from the Hydrology Toolboxes in ArcGIS (e.g. the blue lines in Figure 2 and Figure 3). The preliminary networks, in certain places, are detected to ‘move’ away from their exact locations. The exact layout and location of river channels can be mapped from the high spatial resolution images ( $< 1$  m) obtained from the Google Earth platform, which is accessible by the public. To achieve this, the preliminary networks generated from ArcGIS are converted into Keyhole Markup Language (KML) and then overlaid on Google Earth. The inexact parts are drawn manually on the virtual globe viewing window and then saved on a new KML file. The new KML is imported into ArcGIS and used to replace the inexact parts (i.e. the red lines in Figure 3).

It should be noted that the optimum images displayed in Google Earth may come from different years. To ensure the networks reflecting the hydrological conditions of the specific year under consideration, the corrected networks will be further compared with and verified against the HJ-1A/B CCD images obtained at the same time. If the verification fails, the networks will be corrected or supplemented again in ArcGIS.

### **2.1.2 Processing Approach for Flow Connectivity**

After obtaining the exact positions and layouts of the river networks, the river profiles are

extracted from the DEM. For each river/channel, its profile consists of a series of elevation values from the most upstream point to the outlet along the flow direction. An example is shown in Figure 4a and a number of obstacles impeding flow connectivity are detected in the selected river profile. The line segments containing the three most obvious obstacles are marked within the blue boxes and will be further analyzed in the virtue of Google Earth platform.

For segment 1 (Figure 4b), the channel width is narrow ( $\sim 15$  m) in this reach. With a resolution of  $\sim 90$  m, the center points of DEM pixel fall outside the river and pick up the higher elevation values in the surrounding locations. For example, the points with elevations of 426 m, 425 m, 423 m and 420 m are all located in the riverbank; a few points with higher elevations of 444 m, 454 m, and 457 m are found on the vegetated mountain, as shown in Figure 4b.

For segment 2 as shown in Figure 4c, the points have captured the elevation of a dam and the dam's appendages, which are higher than the upstream points (383 m) and seriously hinder the reservoir outflow. For segment 3 as illustrated in Figure 4d, although the channel reach is wide enough to be captured by the DEM pixels, the center points of the pixels may not coincide with the central line of the river (generally has a lower elevation), which inevitably results in overestimation of channel elevation and subsequently reduces conveyance. Although there are pits in the river profile due to the white noise in the DEM, majority of the obstacles that impede flow connectivity have positive biases due to the surface objects or the offset of river central line in the DEM. Herein, we propose a new approach to remove the positive biases and rebuild flow connectivity for river networks. The positive biases are removed by caving the raised segment.

To maintain a reasonable river slope and terrain harmony between the networks and hillslopes,

the corrected value for every raised river/channel is calculated by taking into account the slope between the nearest upstream pixel and the nearest downstream pixel outside the raised segment (Figure 5). The slope ( $S$ ) and correction value ( $\Delta$ ) are calculated by:

$$S = \frac{Z_{Upstream} - Z_{Downstream}}{N + 1} \quad (1)$$

$$\Delta_i = S * i \quad (2)$$

$$Z_{cor\_i} = Z_i - \Delta_i \quad (3)$$

where  $N$  is the number of pixels contained in the raised segment under consideration,  $Z_{Upstream}$  and  $Z_{Downstream}$  are the elevations of the nearest upstream and downstream pixels outside the raised segment,  $Z_i$  is the elevation of pixel  $i$  before correction where  $i$  is the index of the pixels within the segment,  $Z_{cor\_i}$  the corresponding corrected elevation, and  $\Delta_i$  is the value to be corrected for pixel  $i$ .

In the previous studies, DEMs are mainly corrected using pit removal, which may excessively alter the elevations and destroy the realistic terrains without distinguishing true and false pits. The correction approach proposed in this work identifies the ‘real’ positive biases in the SRTM DEM, followed by caving the positive biases of the raised segment. The correction focuses on the key hydrology features (river/drainage networks) rather than the whole basin to avoid exaggerated modification. Meanwhile, compared with the pit removal method that required manual adjustment (Yamazaki et al., 2012), the current approach is reinforced by the slope condition of the topography in the Multi-Error Removed DEM, which may better represent the realistic terrains.

For each river channel inside the watershed, the raised segments are corrected one by one using the proposed method, from upstream to downstream (Figure 4e). This river profile

correction procedure will be applied to every river and tributary until flow connectivity of the whole river network is guaranteed.

## 2.2 Integrated Hydrologic–Hydraulic Modeling

To simulate the watershed-scale flood evolution, a 2-D hydraulic model is adopted and applied in this study. However, most of the existing hydraulic models are not capable of representing certain key hydrological process, such as evapotranspiration, interception and infiltration. Herein an integrated hydrologic–hydraulic modeling approach is developed and used, in which the surface runoff generated from a rainstorm is generated by a hydrologic model and used as inputs to drive the hydraulic model and create flooding.

### 2.2.1 Hydrologic Modeling

The SCS-CN model is adopted in this work because of its simplicity, stability and success in previous studies for runoff generation (Mishra & Singh, 2007). The models consider most of key watershed characteristics related to runoff generation, including land use, soil type and antecedent moisture condition (Chen et al., 2016). Infiltration models, such as Horton and Green-Ampt methods have been also used together with hydraulic models to predict surface runoff from intense rainfall (Fernández-Pato et al., 2016). But these models commonly require substantial field data for model calibration and verification and are not suitable for the current study.

The SCS-CN model is designed for predicting surface runoff ( $SR$ ) of a specified rainstorm as follows (Mishra and Singh 1999; Woodward et al., 2002):

$$SR = \frac{(P - I_a)^2}{(P - I_a) + S} \quad (4)$$

where  $P$  is the precipitation depth;  $S$  is the maximum potential retention;  $I_a$  is the initial

abstraction defined as  $I_a = \lambda S$  with  $\lambda$  taken as 0.2; and  $S$  is a parameter related to the Curve Number (CN) as follows:

$$S = \frac{2540}{CN} - 25.4 \quad (5)$$

CN is the only parameter in SCS-CN and its value, determined by the watershed characteristics, may be obtained from Section-4 of the National Engineering Handbook (SCS, 1956).

It should be noted that SCS-CN was originally designed to compute the total runoff volume and is not a time-advancing method. In this study, in order to generate runoff volumes that are consistent with the spatial and temporal resolution of the 2-D hydraulic model, SCS-CN is performed at every time step and in every cell of the computational grid that decomposes the computational domain (i.e. the watershed under consideration). According to Caviedes-Voullième et al. (2012), the cumulative surface runoff for a given time is computed from the cumulative precipitation from the beginning of the rainfall event to the specific time being considered; the surface runoff for a specific time step is the increment calculated by subtracting the cumulative runoff from the previous time step.

Consistent with the spatial resolution of the available DEM, SCS-CN is implemented in every  $90 \text{ m} \times 90 \text{ m}$  pixel inside the study area. The cumulative precipitation, antecedent soil moisture, land use and soil type for each pixel are provided or defined at each of the pixels. Herein, hourly cumulative precipitation that drives a simulation is estimated via interpolation from the four closest precipitation stations using the inverse distance squared weighting method. Antecedent soil moisture is determined from the precipitation five days before the flood. Land use data is available from the Global Land Cover Mapping (Chen et al., 2015) and soil type information is derived from the harmonized world soil database (Nachtergaele et al, 2012).



### 2.2.2 2-D Hydraulic Modeling

A fully dynamic hydraulic model based on the 2-D depth-averaged shallow water equations is adopted in this work for flood simulations. The conservative form of the governing 2-D shallow water equations is expressed as follows:

$$\frac{\partial \mathbf{q}}{\partial t} + \frac{\partial \mathbf{f}}{\partial x} + \frac{\partial \mathbf{g}}{\partial y} = \mathbf{s} \quad (6)$$

where  $t$  is the time;  $x$  and  $y$  represent the Cartesian coordinates;  $\mathbf{q}$  denotes the flow variable vector;  $\mathbf{f}$  and  $\mathbf{g}$  are the flux vectors in the  $x$ - and  $y$ -direction, respectively; and  $\mathbf{s}$  is the source term vector. The vector terms are defined as:

$$\mathbf{q} = \begin{bmatrix} h \\ q_x \\ q_y \end{bmatrix} \quad \mathbf{f} = \begin{bmatrix} q_x \\ uq_x + \frac{1}{2}gh^2 \\ uq_y \end{bmatrix}$$

$$\mathbf{g} = \begin{bmatrix} q_y \\ vq_x \\ vq_y + \frac{1}{2}gh^2 \end{bmatrix} \quad \mathbf{s} = \begin{bmatrix} 0 \\ -C_f u \sqrt{u^2 + v^2} - gh \frac{\partial z_b}{\partial x} \\ -C_f v \sqrt{u^2 + v^2} - gh \frac{\partial z_b}{\partial y} \end{bmatrix} \quad (7)$$

where  $h$  is the water depth;  $q_x = uh$  and  $q_y = vh$  are the unit-width discharges in the  $x$ - and  $y$ -directions, respectively;  $u$  and  $v$  denote the depth-averaged velocities in two Cartesian directions; and  $z_b$  is the bed elevation; and  $C_f$  is the bed roughness coefficient.

The above governing equations are solved using a shock-capturing finite volume Godunov-type scheme on uniform grids. Detailed description of the model can be found in Hou et al. (2014) and Xia et al. (2017). To substantially improve its computational efficiency for large-scale flood simulations, the current model is implemented for parallelized computing on multiple GPUs using NVIDIA's parallel computing architecture CUDA (compute unified device architecture). A GPU-accelerated model was reported to be 10s times computationally more efficient than its counterpart running on a CPU (Jarihani et al., 2015).

The 2-D hydraulic model is set up using the available topographic and roughness data and

driven by the hourly surface runoff volumes calculated by SCS-CN at every computational pixel. The runoff is then automatically routed by the hydraulic model within the computational domain before confluence at the basin outlet. The topographic data used in this work include the original DEM, Bare-Earth DEM, Multi-Error DEM, and hydraulically corrected DEM. Roughness of the watershed is indicated by the Manning coefficient ( $n$ ). Standard values of the Manning coefficient corresponding to different watershed characteristics may be found from a hydraulics textbook or report (e.g. [Chow, 1959](#); [Arcement & Schneider, 1984](#)) and using these values in hydraulic modeling has become a common practice (e.g., [Garrote et al., 2016](#)). The Manning coefficients are specified according to different land use types as available from the Global Land Cover Mapping ([Chen et al., 2015](#)), 0.15 for forest, 0.035 for arable land, 0.03 for grassland, 0.027 for water surface and 0.016 for construction land.

Simulation results from the integrated hydrologic-hydraulic model are validated against time histories of water depth measured at gauge stations and inundation extent derived from remotely sensed images. Water depths predicted on different DEMs are evaluated through comparison with gauge records. Predicted flood extents are compared with the flood footprints extracted from the HJ-1A/B imagery based on Normalized Difference Water Index ( $NDWI$ ) ([McFeeters, 1996](#)) and Enhanced Vegetation Index ( $EVI$ ) ([Huete et al., 2002](#)).  $NDWI$  can effectively distinguish water signal against most of the terrestrial and soil features, with  $NDWI$  classified into open water ( $NDWI > 0$ ) and non-water ( $NDWI \leq 0$ ). However, the open water class may not all correspond to flood footprints, because certain places may quickly dry up after being flooded and do not contain open water. Therefore, these “temporally” flooded areas may be missed out by  $NDWI$ , leading to derivation of unreliable flood footprints.  $EVI$  is a widely-

used proxy of vegetation greenness to evaluate the terrestrial photosynthetic activity (Shi et al., 2017). The difference between the *EVI*s before and after a flood event reflects the degree of vegetation being damaged by flood and is a useful indicator for identifying inundated areas. In this work, *NDWI* and *EVI* are used to derive flood extents for evaluating simulation results.

The formulas for calculating *NDWI* and *EVI* are given as follows:

$$NDWI = (R_{Green} - R_{Nir}) / (R_{Green} + R_{Nir}) \quad (8)$$

$$EVI = 2.5 \times (R_{Nir} - R_{Red}) / (R_{Nir} + 6 \times R_{Red} - 7.5 \times R_{Blue} + 1) \quad (9)$$

where  $R_{Nir}$ ,  $R_{Red}$ ,  $R_{Green}$ , and  $R_{Blue}$  are referred as the reflectance of the near-infrared, red, green and blue bands of HJ-1A/B CCD images, respectively.

### 3 RESULTS AND DISCUSSION

#### 3.1 Study Area and the Flood Event

A 267 km reach of the Huifa River in the northeastern China (Figure 2) is selected as the case study. Approximately 33% of the total areas are covered by forests with clear spatial variation, making it an ideal site for investigating the influence of vegetation bias in the original SRTM DEM on flood modeling. The river networks are characterized by numerous tributaries and sub-pixel sized channels and their representation is particularly sensitive to DEM quality and important for flood modeling, providing a desired case study to test the applicability of the hydraulically improved DEM for use in 2-D hydraulic flood modeling. Detailed hydrometeorological data are available for the study site, including rainfall records from 253 precipitation stations and continuous water depth measurements from 8 hydrologic stations along the main channel reach. Meanwhile, HJ-1A/B CCD images are available to derive the

actual flooded areas.

The Huifa River has a basin area of 14,896 km<sup>2</sup> and is mainly located in Jilin Province, northeastern China. The local climate is dominated by continental monsoons. With an annual average of 720 mm, the rainfall has a clear seasonal variation. Rainfall occurs mostly during summer and autumn and 44.7 % of the annual total is recorded in July and August (Zhang et al., 2012). Corresponding to the seasonal rainfall variation, there is a clearly defined flood season from June to September and a dry period from October to the following May. According to gauge station records, during 1965-2015, the mean discharge of Huifa River is 83.70 m<sup>3</sup>/s and the maximum peak discharge is measured to be 3410 m<sup>3</sup>/s, occurring during the flood season in 2013. The 2013 extreme flood event will be further investigated in this study.

In August 2013, an area average rainfall of 221 mm was recorded in the Huifa River Basin, leading to an extreme flood event with a 50-year return period (Jin et al., 2015). The flood caused disastrous consequences in all three Northeast provinces, i.e. Heilongjiang, Jilin and Liaoning. According to the Ministry of Civil Affairs, approximately 5 million people were affected; 95 people were killed; 154,622 houses were damaged; and 1.59 million hectares of croplands were affected (Hong Kong Red Cross, 2013).

### **3.2 Hydraulically Corrected SRTM DEM**

Using ArcGIS, Google Earth and HJ-1A/B CCD images, we acquire the ‘exact’ layout and locations of the river networks in the Huifa River basin (Figure 3). The river networks consist of a total of 312 tributaries, with length ranging from 0.5 kilometers to 267 kilometers. River networks may be quickly generated from a DEM using ArcGIS. However, the resulting networks may contain obvious inaccuracies in both location and layout, which may be easily

detected by overlaying the derived networks with Google Earth images. In flood modeling, flow connectivity of the river networks is a key factor affecting the simulation results. It is necessary to correct the river networks derived directly from a DEM to support more reliable flood predictions. The availability of Google Earth at high spatial resolution and HJ-1A/B CCD images has provided an opportunity to resolve the issue. By combining ArcGIS, Google Earth with the timely remote sensing images, we may now accurately position river networks and improve their flow connectivity in basins of different scales.

Herein the proposed HCM is used to ensure flow connectivity of the river networks in the Huifa River basin. Among the 2349,401 pixels of the Multi-Error Removed DEM inside the basin, 37,032 pixels (1.6%) pixels are identified to form raised segments breaking the flow connectivity of the river networks. The amount of correction as required is less than 1 m at 14,025 pixels (38%) and less than 2 m at 26,551 pixels (72%). In all of the modified pixels, 95% of them require correction of less than 4 m. The average amount of correction is only 46 mm for the whole basin. *Supporting Material* Figure S1 shows the 6 main channels (see in Figure 2) in the study area. It is observed that the overall topographic features of all 6 channels are well maintained following flow connectivity reconstruction. Meanwhile, when the elevations of the channel pixels are adjusted to more reasonable values, the exchange of flow between hillslopes and river networks may be better depicted in 2-D hydraulic modeling.

### **3.3 Validation of Simulation Results with in Suit Measured Water Depths**

To validate the flood simulation results on the four DEMs as considered in this work, the surface runoff generated from SCS-CN is compared with the discharge measured in the Wudaogou station near the basin outlet (see *Supporting Material* Figure S2); and the water depths

calculated by the 2-D hydraulic model are compared with the measurements available at the eight gauge stations within the model domain (see Figure 2). The eight gauge stations are located along the main tributaries, with contributing basin areas varying from 150 km<sup>2</sup> to 2000 km<sup>2</sup> (Table 1). The predicted and measured hourly hydrographs of water depth are shown in Figure 6 for all eight stations. The calculated root mean square errors (RMSE) and the difference between the predicted and measured maximum water depths (DI) are summarized in Table 1.

The total runoff volume computed from SCS-CN is  $1.36 \times 10^9$  m<sup>3</sup>, the actual volume measured in the Wudaogou station is  $1.52 \times 10^9$  m<sup>3</sup>. The error between the computed and measured is approximately 11%, which is acceptable. This also confirms that the adopted CN numbers (derived based on the watershed characteristics and previous research) are reasonable. The depth hydrographs calculated on the original DEM represented by the red lines in Figure 6 and the Bare-Earth DEM and Multi-Error Removed DEM represented by yellow lines and green lines respectively in Figure 6 are somehow similar, with peak water depth underestimated at almost all eight stations. At stations 1, 2, 5 and 8, the predicted depth hydrographs feature a correct rising-falling process. However, the magnitudes of the predicted depths are not consistent with the observations and the peak water depths predicted on the original DEM are approximately 0.3 m larger than those predicted on the Bare-Earth DEM. This may be because the Bare-Earth DEM has lower elevation values after removing vegetation bias (vegetation bias removal effectively makes the DEM values to become the same level as the surrounding topography), leading to more flood water detained on the hillslopes and less water discharged to stream outlets. The Multi-Error Removed DEM performs better in predicting the peak water

depths than the original DEM and the Bare-Earth DEM at stations 1, 5 and 8. At stations 3 and 6, simulations on the original DEM, Bare-Earth DEM, and Multi-Error Removed DEM all predict a dry river with no water depth. The correct water depth hydrograph is not reproduced because the water flow cannot move from upstream to the gauge station as a result of blocked channel and broken flow connectivity. At stations 4 and 7, the water depth suddenly increases and then maintains at a constant depth. This suggests that the DEMs have turned both of the locations to become pits. As a result, the flood water maintains at a constant level after the pits are quickly filled.

Comparing the depth hydrographs predicted on the hydraulically corrected DEM with those predicted on the other three DEMs shows that, at most of the stations, the corrected DEM performs better in predicting the rise-and-fall process of water depth and peak water depth. The results from the corrected DEM indicate that the model has succeeded in depicting the rising-falling process of the water depth at all eight stations. Except for stations 7 and 8, the peak water depths predicted on the corrected DEM agree more closely with the observed values and higher than those predicted on the other three DEMs. This is because the predicted water flow successfully propagates from upstream to the outlet through the connecting networks, which are better represented in the corrected DEM via the correcting method outlined in the previous section. It needs to be noted that the simulation on the corrected DEM overestimates the peak water depth at station 8. The reason may be that the river channel becomes smoothed following the DEM correction process, leading to reduced retention volume. Another possible reason may be because the storage of reservoirs is not considered in the current study. The results demonstrate that improved 2-D flood modeling can be achieved by better depicting the

connected channels using the hydraulic correction method as proposed in this study to process a DEM.

### 3.4 Validation of Simulation Results with Remote Sensing Images

The inundation extent predicted by the 2-D hydraulic model is compared with the satellite observations of flood footprint obtained from the HJ-1A/B CCD images. Two HJ images are used. One was acquired during the flood period on 23 August 2013 and another was acquired before the flood event on 6 July 2013. Based on the *NDWI* ( $> 0$ ) calculated from the image during flood period, the surface water area can be identified, including rivers, lakes and ponding areas. However, the surface water area may be significantly less than the actual inundation area because flood water can pass certain regions without forming open water (i.e. boundaries of inundated areas) (Mohammadi et al., 2017). So the vegetation response is also adopted to obtain the flood footprint by identifying the changes in *EVI* values. The ratio of *EVI*s after and before the flood event is calculated for every pixel. We then extract the pixels in which the vegetation has been negatively influenced by the flood event ( $EVI_{\text{after}}/EVI_{\text{before}} < 0.35$  and  $EVI_{\text{before}} > 0$ ). The *EVI* ratio of 0.35 is taken to extract the pixels that are obviously influenced by flooding. The natural fluctuations (e.g. the *EVI* of crop may slightly decrease from before the flood event corresponding to peak growth stage to after the flood event corresponding to mature stage) are excluded to ensure that pure flood footprints are acquired. Considering the fact that certain flood footprints may not involve either water response or vegetation response, satellite observations of flood footprints from the HJ-1A/B CCD images cannot present all areas that are inundated by flood water. We therefore separately analyze the simulation performance to reflect the water response and vegetation response.



For the surface water area, the ratio of overlap areas (ROA) is used to assess simulation performance in predicting open water. ROA is defined as the ratio between the HJ and simulation overlapping area and the HJ surface water area. To evaluate the performance spatially, we compute ROA in every window containing 4x4 pixels (Figure 7b, 7c and 7d) and count ROA values within the 12 sub-basins (Figure 7a and Table 2). Similar results are obtained for the original DEM and Bare-Earth DEM simulations, thus the result drawing of Bare-Earth DEM is not shown in Figure 7 due to space limitation. In Huifa River Basin, vegetation removal (Bare-Earth DEM) shows no improvement in accuracy for predicting open water areas compared with the use of original DEM. Instead, the resulting simulation performance is observed to deteriorate in certain sub-basins, such as sub-basin 9 and 12. On the other hand, hydraulic flood simulation on the Multi-Error Removed DEM shows obvious improvement in almost all sub-basins. The overall accuracy of predicting surface water areas against the HJ image has been improved from a ROA of 0.67 (original DEM) and 0.65 (Bare-Earth DEM) to 0.71 (Multi-Error Removed DEM). Among all the four DEMs, the hydraulically corrected DEM performs the best in predicting surface water areas in the whole basin and all sub-basins. The overall accuracy of predicting surface water areas against the HJ image rises to 0.79. Comparison between these predicted surface water areas visually shows that simulations on the original DEM and Bare-Earth DEM only correctly predict inundation in a few small areas in the midstream, including the corresponding main channel, and sub-basins 5, 6 and 11 (~ 40%), whereas the simulation on the Multi-Error Removed DEM and the corrected DEM show a marked improvement, and the corrected DEM accurately predicts most of the observed water surface areas (~ 70%). This implies that well-connected river networks ensure flow connectivity

and lead to improved flood prediction discharge of the water flow alongside the networks.

To evaluate the performance of simulation results in terms of representing the vegetation response to the flood event, the predicted flood map is assessed through comparison with the areas with vegetation response. The pixels with vegetation response are typically located at the boundaries of open water areas, which are mainly covered by grain crops. According to [Ganji et al. \(2012\)](#), when the inundation depth is more than 0.2 m, crop yield will be obviously affected. So we count the percentage of the predicted maximum water depth more than 0.2 m in the areas with vegetation response (Table 3 and Figure 8). The percentage of water depth more than 0.2 m, increases from 44% predicted on the original DEM and 55% on the Multi-Error Removed DEM to 61% on the corrected DEM for the whole basin. The evidently improved prediction of flooded areas are concentrated on the downstream, which indicates that better connected river networks can lead to better representation of overbank flows along the river channels.

### 3.5 Discussions

The results comparison, obtained from simulations on the original DEM and Bare-Earth DEM, shows that these DEMs give similar results. It means that vegetation removal does not bring obvious improvement for 2-D hydraulic modeling in Huifa River Basin. However, previous related studies in Amazon River basin indicated that SRTM vegetation removal could greatly improve the hydrodynamic modeling accuracy ([Wilson et al., 2007](#); [Baugh et al., 2013](#)). A possible reason for the difference may be because our study area is a mountainous watershed with high vegetation, i.e. forest, is mainly distributed in areas with high slopes, thus vegetation removal does not cause any major change to the relative topographic conditions (e.g. the

average slope of basin only changes from 5.78° to 5.70° after vegetation removal). Subsequently vegetation removal does not impose significant change to the flow connectivity between hillslopes and river channels. This is the reason that we do not focus more on vegetation removal method in this study and just use a generated data set. Meanwhile, in comparison with the Amazon River basin, the current study area consists of relatively fragmented fields and this may also be another reason for the limited improvement in the simulation accuracy. The Bare-Earth DEM (O'Loughlin et al., 2016) was obtained from the 250 m MODIS Vegetation Continuous Field product (DiMiceli et al., 2011) as a proxy of vegetation signal and the 1 km global vegetation height map (Simard et al., 2011). The resolution of these vegetation data may be capable of capturing the spatial heterogeneity of vegetation height in Amazon floodplain covered by more uniformly distributed rainforests, but is may be too coarse for the Huifa basin with smaller fields and different types of forests (Zhang et al., 2008). Therefore, the necessity of vegetation removal for SRTM DEM in 2-D hydraulic modeling should be considered together with the specific watershed conditions of the study area under consideration. More research case studies need to be done to examine the applicability and performance of Bare-Earth DEM in 2-D flood modeling.

Although vegetation bias removal does not bring improvement for 2-D hydraulic modeling, the Multi-Error Removed DEM achieves obvious improvement in predicting inundation areas with water response and vegetation response. We find that the flatness of the topography in flat areas (floodplain) is recovered well to some extent. Moreover, some abnormal bulges and depressions in river stream have been removed and thus the flow connectivity of streams have been improved compared to the original DEM and the Bare-Earth DEM. Thus the flow

connectivity inside the floodplains and the river networks as key factors affecting the simulation results are depicted more realistically. Significant improvement is observed in simulating spatial flood extent. In addition, in predicting the water depths hydrographs of the river channel, both the Bare-Earth DEM and Multi-Error Removed DEM achieve poor performance. It is due to the spatial resolution of DEM itself, which is not fine enough to represent most of the hydrologic features in the study area.

Reconstructing the flow connectivity of river channels on the Multi-Error Removed DEM increases the simulation accuracy of depth hydrographs and inundation areas with water response and vegetation response, comparing with the original DEM, the Bare-Earth DEM, and the Multi-Error Removed DEM. The improved model performance is a result of better representation of channel connectivity, leading to better simulation of overbank flows and flow propagation from upstream channels to the outlets. However, simulations on the corrected DEM have constantly led to overestimation of outflow volume, in comparison with the observations. This overestimation may result from the internal errors of SRTM DEM. For example, the SRTM DEM is not able to accurately capture the river and lake bathymetries below the water surface; the DEM only shows their corresponding water surface elevation, overestimating the bottom elevation of water bodies (Neal et al., 2012; Mersel et al., 2013; Alfieri et al., 2014). This essentially reduces the detention capacity of the water bodies and forces more water flowing to the outlets. Meanwhile, the hydraulic correction method proposed in this work for rebuilding flow connectivity may also contribute to overestimation of outflow volume.

Due to the lack of detailed and accurate river bottom elevation, the river channels are processed according to the slope defined between the upstream point and the downstream point.

Thus the processed channels become smoother than the ‘original’ one. This, to certain extent, may result in less water intercepted in the river channels and consequently more outflow. In spite of the limitations, the proposed approach has great potential for application in watersheds where high-resolution DEMs and detailed channel cross-sections are not available. Since the SRTM DEM and Google Earth platform is (nearly) globally available and the reconnection process after getting the river stream map does not require manual adjustment, it provides a simple and effective approach to improve the applicability of SRTM DEM in 2-D hydraulic flood modeling. Even so, we must admit that when high-accuracy map of river streams is not available, manual corrections and additions of networks from high-resolution Google Earth imagery are time-consuming and not realistic to do globally. New methods are essential to be developed in the following studies to extract global high-precision streams and reduce the processing burden of correction. Fortunately, the previous studies, aimed at extracting large-scale streams from remote sensing imagery not DEM data, may be helpful. For example, [Orengo et al., \(2017\)](#) and [Isikdogan et al., \(2015\)](#) proposed automated methods that extract streams from remote sensing imagery; [Isikdogan et al., \(2017\)](#) developed an automated river mapping engine, which enables the computation of large-scale streams from Landsat data. The streams from remote sensing imagery may be more accurate than the DEM-derived. It can help to reduce the processing burden of correction and then more easily improve the utility of SRTM DEM in global flood simulation.

Besides DEMs, another crucial factor that may affect the performance of hydraulic model in modeling floods is related to the specification of the Manning’s roughness coefficient ([Neal et al., 2015](#); [Fernández et al., 2016](#)). Optimizing Manning’s coefficient may further improve

model performance. Specifically, calibrating the Manning's coefficient may have a great influence on flood arrival time and attenuation. To further investigate the role of Manning's coefficient in 2-D hydraulic modeling, further simulations have been run, but only in the sub-catchments of Huifa Basin in order to reduce computational cost. Simulation results suggest that the use of different Manning's coefficient does not have a big effect on the conclusions related to the performance of the four DEMs in supporting 2-D hydraulic modeling, providing that the Manning's coefficient is chosen from a reasonable range. Thus, in this study, the Manning's coefficient used in the simulations is directly determined according to land cover types, basin characteristics and also previous studies.

#### **4 CONCLUSIONS**

A hydraulic correction method (HCM) is proposed in this study to overcome the limitations (vegetation bias, random errors, and insufficient spatial resolution) of the SRTM DEM in 2-D hydraulic modeling. A comparative analysis is performed to investigate the simulation accuracy obtained on the original DEM, Bare-Earth DEM, Multi-Error Removed DEM, and hydraulically corrected DEM. On the four DEMs, an extreme flood event occurred in the 14,896 km<sup>2</sup> Huifa River Basin has been systematically simulated and reproduced using the combined SCS-CN hydrological and 2-D hydraulic model developed in this work. The modeling results indicated that:

- (a) Vegetation removal does not bring any obvious improvement when comparing water depth hydrographs and inundation areas with water response and vegetation response obtained from different simulations; removal of height errors, including vegetation bias and random

errors brings obvious improvement in predicting inundation areas;

(b) The hydraulically corrected DEM performs better in replicating the rising-falling process of the depth hydrographs and capturing the observed peak water depth than the original DEM, Bare-Earth DEM, and Multi-Error Removed DEM;

(c) The corrected DEM ensures river networks to have better flow connectivity and continuous water flow (discharge) along the channels. This improves simulation accuracy. The simulated surface water areas are better consistent with the HJ imagery, with the overlap ratio increasing from 0.67 (original DEM), 0.65 (Bare-Earth DEM), and 0.71 (Multi-Error Removed DEM) to 0.79 (hydraulically corrected DEM);

(d) Overbank flow is more reliably simulated and represented on the corrected DEM with well-connected river networks. The percent of the simulated water depth ( $> 0.2$  m) in the areas with vegetation response from flood has increased from 44% (original DEM) 42% (Bare-Earth DEM), and 55% (Multi-Error Removed DEM) to 61% (hydraulically corrected DEM).

## ACKNOWLEDGMENTS

This work is supported by the National Basic Research Program of China (2015CB458900), National Science Foundation of China (51721006), and the open fund of Ministry of Education Laboratory for Earth Surface Processes.

## REFERENCES

Alexander, L. V., Zhang, X., Peterson, T. C., Caesar, J., Gleason, B., & Klein Tank, A. M. G., et al. (2006). Global observed changes in daily climate extremes of temperature and precipitation. *Journal of Geophysical Research Atmospheres*, 111(D5), 1042-1063.

Alfieri, L., Salamon, P., Bianchi, A., Neal, J., Bates, P., & Feyen, L. (2014). Advances in pan-European flood hazard mapping. *Hydrological Processes*, 28(13), 4067-4077.

Alsdorf, D. E., Rodriguez, E., & Lettenmaier, D. P. (2007). Measuring surface water from space. *Reviews of Geophysics*, 45(2).

Arcement, G. J., & Schneider, R. (1984). Guide for selecting manning's roughness coefficients for natural channels and floodplains. *Roughness Coefficient*.

Arnold, J. G., Srinivasan, R., Muttiah, R. S., & Williams, J. R. (1998). Large area hydrologic modeling and assessment part I: model development. *Jawra Journal of the American Water Resources Association*, 34(1), 73–89.

Athmania, D., & Achour, H. (2014). External validation of the ASTER GDEM2, GMTED2010 and CGIAR-CSI-SRTM v4. 1 free access digital elevation models (DEMs) in Tunisia and Algeria. *Remote Sensing*, 6(5), 4600-4620.

Barnes, H. H. (1967). Roughness characteristics of natural channels. *Center for Integrated Data Analytics Wisconsin Science Center*.

Bates, P. D., Horritt, M., & Hervouet, J. M. (1998). Investigating two-dimensional, finite element predictions of floodplain inundation using fractal generated topography. *Hydrological processes*, 12(8), 1257-1277.

Baugh, C. A., Bates, P. D., Schumann, G., & Trigg, M. A. (2013). SRTM vegetation removal and hydrodynamic modeling accuracy. *Water Resources Research*, 49(9), 5276-5289.

Brown, C. G., Sarabandi, K., & Pierce, L. E. (2010). Model-based estimation of forest canopy height in red and Austrian pine stands using Shuttle Radar Topography Mission and ancillary data: a proof-of-concept study. *IEEE Transactions on Geoscience & Remote Sensing*, 48(3), 1105-1118.

Callow, J. N., Niel, K. P. V., & Boggs, G. S. (2007). How does modifying a DEM to reflect known hydrology affect subsequent terrain analysis?. *Journal of Hydrology*, 332(1–2), 30-39.

Carabajal, C. C., & Harding, D. J. (2005). ICESat validation of SRTM C-band digital elevation models. *Geophysical research letters*, 32(22).

Caviedes-Voullième, D., García-Navarro, P., & Murillo, J. (2012). Influence of mesh structure on 2D full shallow water equations and SCS Curve Number simulation of rainfall/runoff events. *Journal of Hydrology*, 448, 39-59.

Chaieb, A., Rebai, N., & Bouaziz, S. (2016). Vertical Accuracy Assessment of SRTM Ver 4.1 and ASTER GDEM Ver 2 Using GPS Measurements in Central West of Tunisia. *Journal of Geographic Information System*, 8(01), 57.

Chen, H., Liang, Z., Liu, Y., Liang, Q., & Xie, S. (2017). Integrated remote sensing imagery and two-dimensional hydraulic modeling approach for impact evaluation of flood on crop yields. *Journal of Hydrology*, 553, 262-275.



Chen, L., Gong, Y., & Shen, Z. (2016). Structural uncertainty in watershed phosphorus modeling: toward a stochastic framework. *Journal of Hydrology*, 537, 36-44.

Chen, L., Sun, C., Wang, G., Xie, H., & Shen, Z. (2017b). Event-based nonpoint source pollution prediction in a scarce data catchment. *Journal of Hydrology*, 552.

Chen, J., Chen, J., Liao, A., Cao, X., Chen, L., & Chen, X., et al. (2015). Global land cover mapping at 30 m resolution: a POK-based operational approach. *ISPRS Journal of Photogrammetry & Remote Sensing*, 103, 7-27.

Cheng, G., Dong, C., Huang, G., Baetz, B. W., & Han, J. (2016). Discrete principal - monotonicity inference for hydro - system analysis under irregular nonlinearities, data uncertainties, and multivariate dependencies. Part I: methodology development. *Hydrological Processes*, 30(23), 4255-4272.

Cheng, G., Dong, C., Huang, G., Baetz, B. W., & Han, J. (2016). Discrete principal - monotonicity inference for hydro-system analysis under irregular nonlinearities, data uncertainties, and multivariate dependencies. Part II: application to streamflow simulation in the Xingshan watershed, China. *Hydrological Processes*, 30(23), 4273-4291.

Cheng, G. H., Huang, G. H., Dong, C., Zhu, J. X., Zhou, X., & Yao, Y. (2017a). An evaluation of CMIP5 GCM simulations over the Athabasca River Basin, Canada. *River Research & Applications*, 33(5), 823-843.

Cheng, G., Huang, G., Dong, C., Zhu, J., Zhou, X., & Yao, Y. (2017b). High - resolution projections of 21st century climate over the Athabasca River Basin through an integrated evaluation-classification-downscaling-based climate projection framework. *Journal of Geophysical Research*, 122(5), 2595-2615.

Cheng, G., Huang, G., Dong, C., Zhu, J., Zhou, X., & Yao, Y. (2017c). Recursive multivariate principal-monotonicity inferential climate downscaling. *Quarterly Journal of the Royal Meteorological Society*, online press.

Cheng, G., Huang, G., Dong, C., Zhou, X., Zhu, J., & Xu, Y. (2017d). Climate classification through recursive multivariate statistical inferences: a case study of the Athabasca River Basin, Canada. *International Journal of Climatology*, 37, 1001-1012.

Chow, V.T., 1959. Open-channel Hydraulics. McGraw-Hill, Book Co., New York, p. 680.

Coe, M. T., Costa, M. H., & Howard, E. A. (2010). Simulating the surface waters of the Amazon River basin: impacts of new river geomorphic and flow parameterizations. *Hydrological Processes*, 22(14), 2542-2553.

DiMiceli, C. M., Carroll, M. L., Sohlberg, R. A., Huang, C., Hansen, M. C., & Townshend, J. R. G. (2011). Annual global automated MODIS vegetation continuous fields (MOD44B) at 250 m spatial resolution for data years beginning day 65, 2000-2010, collection 5 percent tree cover. *University of Maryland, College Park, MD, USA*.

- Dottori, F., Salamon, P., Bianchi, A., Alfieri, L., Hirpa, F. A., & Feyen, L. (2016). Development and evaluation of a framework for global flood hazard mapping. *Advances in Water Resources*, 94, 87-102.
- European Commission, 2007. Directive 2007/60/EC of the European Parliament and of the Council of 23 October 2007 on the assessment and management of flood risks. Official J. Eur. Union L 288, 27–34.
- Falorni, G., Teles, V., Vivoni, E. R., Bras, R. L., & Amaratunga, K. S. (2005). Analysis and characterization of the vertical accuracy of digital elevation models from the Shuttle Radar Topography Mission. *Journal of Geophysical Research: Earth Surface*, 110(F2).
- Farr, T. G., Rosen, P. A., Caro, E., Crippen, R., Duren, R., & Hensley, S., et al. (2007). The shuttle radar topography mission. *Reviews of Geophysics*, 45(2), 361.
- Fernández, A., Najafi, M. R., Durand, M., Mark, B. G., Moritz, M., & Jung, H. C., et al. (2016). Testing the skill of numerical hydraulic modeling to simulate spatiotemporal flooding patterns in the Logone floodplain, Cameroon. *Journal of Hydrology*, 539, 265-280.
- Fujisada, H., Urai, M., & Iwasaki, A. (2012). Technical methodology for ASTER global DEM. *IEEE Transactions on Geoscience and Remote Sensing*, 50(10), 3725-3736.
- Gallant, J. C., & Read, A. (2009). Enhancing the SRTM data for Australia. *Proceedings of geomorphometry*, 31, 149-154.
- Ganji, Z., Shokoohi, A., & Samani, J. M. (2012). Developing an agricultural flood loss estimation function (case study: rice). *Natural hazards*, 64(1), 405-419.
- Garrote, J., Alvarenga, F. M., & Díez-Herrero, A. (2016). Quantification of flash flood economic risk using ultra-detailed stage–damage functions and 2-d hydraulic models. *Journal of Hydrology*, 541, 611-625.
- Hirt, C., Filmer, M. S., & Featherstone, W. E. (2010). Comparison and validation of the recent freely available ASTER-GDEM ver1, SRTM ver4. 1 and GEODATA DEM-9S ver3 digital elevation models over Australia. *Australian Journal of Earth Sciences*, 57(3), 337-347.
- Hong Kong Red Cross, (2013). China Floods 2013: Work Report 4. Retrieved August 30, 2013, from [http://www.redcross.org.hk/en/disasterrelief\\_prepared/appeal\\_update\\_detail.html?year=2013&id=1654](http://www.redcross.org.hk/en/disasterrelief_prepared/appeal_update_detail.html?year=2013&id=1654).
- Hou, J., Simons, F., Liang, Q., & Hinkelmann, R. (2014). An improved hydrostatic reconstruction method for shallow water model. *Journal of Hydraulic Research*, 52(3), 432-439.
- Huete, A., Didan, K., Miura, T., Rodriguez, E. P., Gao, X., & Ferreira, L. G. (2002). Overview of the radiometric and biophysical performance of the MODIS vegetation

indices. *Remote Sensing of Environment*, 83(1-2), 195-213.

Isikdogan, F., Bovik, A., & Passalacqua, P. (2015). Automatic channel network extraction from remotely sensed images by singularity analysis. *IEEE Geoscience & Remote Sensing Letters*, 12(11), 2218-2221.

Isikdogan, F., Bovik, A., & Passalacqua, P. (2017). Rivamap: an automated river analysis and mapping engine. *Remote Sensing of Environment*, 202, 88–97.

Jarihani, A. A., Callow, J. N., McVicar, T. R., Van Niel, T. G., & Larsen, J. R. (2015). Satellite-derived Digital Elevation Model (DEM) selection, preparation and correction for hydrodynamic Modeling in large, low-gradient and data-sparse catchments. *Journal of Hydrology*, 524, 489-506.

Jenson, K., & Domingue, O. (1988). Extracting topographic structure from digital elevation data for geographic system analysis. *Sensing*, 54(11), 1593--1600.

Jin, C., Li, W., & Li, X. (2015). Research and thinking of flood forecast in Northeast China. *Water Resources & Hydropower of Northeast China*, 33(12), 38-41. (In Chinese)

Jing, C., Shortridge, A., Lin, S., & Wu, J. (2014). Comparison and validation of SRTM and ASTER GDEM for a subtropical landscape in Southeastern China. *International Journal of Digital Earth*, 7(12), 969-992.

Kenny, F., Matthews, B., & Todd, K. (2008). Routing overland flow through sinks and flats in interpolated raster terrain surfaces. *Computers & Geosciences*, 34(11), 1417-1430.

Khakbaz, B., Imam, B., Hsu, K., & Sorooshian, S. (2012). From lumped to distributed via semi-distributed: calibration strategies for semi-distributed hydrologic models. *Journal of Hydrology*, 418–419(4), 61-77.

Khan, U.T & Valeo, C. (2016). Short-Term Peak Flow Rate Prediction and Flood Risk Assessment Using Fuzzy Linear Regression. *Journal of Environmental Informatics*, 28(2), 71-89.

Kiel, B., Alsdorf, D., & LeFavour, G. (2006). Capability of SRTM C-and X-band DEM data to measure water elevations in Ohio and the Amazon. *Photogrammetric Engineering & Remote Sensing*, 72(3), 313-320.

Kim, J., Warnock, A., Ivanov, V. Y., & Katopodes, N. D. (2012). Coupled modeling of hydrologic and hydrodynamic processes including overland and channel flow. *Advances in Water Resources*, 37(1), 104-126.

Lalonde, T., Shortridge, A., & Messina, J. (2010). The influence of land cover on shuttle radar topography mission (SRTM) elevations in low-relief areas. *Transactions in Gis*, 14(4), 461–479.

Lee, C., Kim, K., Park, Y., & Lee, H. (2017). GIS-based reach file generation for efficient

TMDLs implementation. *Journal of Environmental Informatics*, 28(1), 45-60.

Lefsky, M. A. (2010). A global forest canopy height map from the Moderate Resolution Imaging Spectroradiometer and the Geoscience Laser Altimeter System. *Geophysical Research Letters*, 37(15).

Lehner, B., Verdin, K., & Jarvis, A. (2008). New global hydrography derived from spaceborne elevation data. *Eos, Transactions American Geophysical Union*, 89(10), 93-94.

Lu, Y., Qin, X. S., & Xie, Y. J. (2016). An integrated statistical and data-driven framework for supporting flood risk analysis under climate change. *Journal of Hydrology*, 533, 28-39.

Luo, X., Hong-Yi, L., Leung, L. R., Tesfa, T. K., Getirana, A., Papa, F., & Hess, L. L. (2017). Modeling surface water dynamics in the Amazon Basin using MOSART-Inundation v1.0: impacts of geomorphological parameters and river flow representation. *Geoscientific Model Development*, 10(3), 1233.

Martz, L. W., & Garbrecht, J. (1999). An outlet breaching algorithm for the treatment of closed depressions in a raster DEM. *Computers & Geosciences*, 25(7), 835-844.

Masutomi, Y., Inui, Y., Takahashi, K., Matsuoka, Y., Yamashiki, Y., & Tsujimura, M. (2009). Development of highly accurate global polygonal drainage basin data. *Hydrological Processes*, 23(4), 572-584.

McFeeters, S. K. (1996). The use of the Normalized Difference Water Index (NDWI) in the delineation of open water features. *International journal of remote sensing*, 17(7), 1425-1432.

Mersel, M. K., Smith, L. C., Andreadis, K. M., & Durand, M. T. (2013). Estimation of river depth from remotely sensed hydraulic relationships. *Water Resources Research*, 49(6), 3165-3179.

Mishra, S. K., & Singh, V. P. (1999). Another look at SCS-CN method. *Journal of Hydrologic Engineering*, 4(3), 257-264.

Mishra, S. K., & Singh, V. P. (2007). Soil conservation service curve number (SCS-CN) methodology. *Water Science & Technology Library*, 22(3), 355-362.

Mohammadi, A., Costelloe, J. F., & Ryu, D. (2017). Application of time series of remotely sensed normalized difference water, vegetation and moisture indices in characterizing flood dynamics of large-scale arid zone floodplains. *Remote Sensing of Environment*, 190, 70-82.

Mtamba, J., Velde, R. V. D., Ndomba, P., Zoltán, V., & Mtalo, F. (2015). Use of Radarsat-2 and Landsat tm images for spatial parameterization of manning's roughness coefficient in hydraulic modeling. *Remote Sensing*, 7(1), 836-864.

Nachtergaele, F. O., Velthuisen, Verelst, L., Batjes, N. H., Dijkshoorn, J. A., & Engelen, et al. (2012). Harmonized world soil database (version 1.2).

- Neal, J. C., Odoni, N. A., Trigg, M. A., Freer, J. E., Garcia-Pintado, J., & Mason, D. C., et al. (2015). Efficient incorporation of channel cross-section geometry uncertainty into regional and global scale flood inundation models. *Journal of Hydrology*, 529(1), 169-183.
- Neal, J., Schumann, G., & Bates, P. (2012). A subgrid channel model for simulating river hydraulics and floodplain inundation over large and data sparse areas. *Water Resources Research*, 48(11), 11506.
- Nguyen, P., Thorstensen, A., Sorooshian, S., Hsu, K., Aghakouchak, A., & Sanders, B., et al. (2015). A high resolution coupled hydrologic-hydraulic model (hiresflood-uci) for flash flood modeling. *Journal of Hydrology*, 541, 401-420.
- O'Loughlin, F. E., Paiva, R. C. D., Durand, M., Alsdorf, D. E., & Bates, P. D. (2016). A multi-sensor approach towards a global vegetation corrected SRTM DEM product. *Remote Sensing of Environment*, 182, 49-59.
- Orengo, H. A., & Petrie, C. A. (2017). Large-scale, multi-temporal remote sensing of Palaeo-River networks: a case study from northwest India and its implications for the Indus Civilisation. *Remote Sensing*, 9(7), 735.
- Paiva, R. C. D. D., Buarque, D. C., Collischonn, W., Bonnet, M. P., Frappart, F., & Calmant, S., et al. (2013). Large-scale hydrologic and hydrodynamic modeling of the Amazon River basin. *Water Resources Research*, 49(3), 1226-1243.
- Paiva, R. C., Collischonn, W., & Tucci, C. E. (2011). Large scale hydrologic and hydrodynamic modeling using limited data and a GIS based approach. *Journal of Hydrology*, 406(3), 170-181.
- Pan, F., Stieglitz, M., & McKane, R. B. (2012). An algorithm for treating flat areas and depressions in digital elevation models using linear interpolation. *Water Resources Research*, 48(6).
- Perrin, C., Michel, C., & Andréassian, V. (2003). Improvement of a parsimonious model for streamflow simulation. *Journal of Hydrology*, 279(1-4), 275-289.
- Pinel, S., Bonnet, M. P., Joecila, S. D. S., Moreira, D., Calmant, S., & Satgé, F., et al. (2015). Correction of interferometric and vegetation biases in the srtmg11 spaceborne DEM with hydrological conditioning towards improved hydrodynamics modeling in the amazon basin. *Remote Sensing*, 7(12), 16108-16130.
- Quintana-Seguí P, Peral M. C, Turco M, Llasat M -C, & Martin E. (2016). Meteorological analysis systems in north-east Spain: validation of SAFRAN and SPAN. *Journal of Environmental Informatics*, 27(2), 116-130.
- Rabus, B., Eineder, M., Roth, A., & Bamler, R. (2003). The shuttle radar topography mission—a new class of digital elevation models acquired by spaceborne radar. *Isprs Journal of Photogrammetry & Remote Sensing*, 57(4), 241-262.

Re, M., 2014. NatCat SERVICE Database. Munich RE, Munich

Rexer, M., & Hirt, C. (2014). Comparison of free high resolution digital elevation data sets (ASTER GDEM2, SRTM v2. 1/v4. 1) and validation against accurate heights from the Australian National Gravity Database. *Australian Journal of Earth Sciences*, 61(2), 213-226.

Saghafian, B., Farazjoo, H., Bozorgy, B., & Yazdandoost, F. (2008). Flood intensification due to changes in land use. *Water Resources Management*, 22(8), 1051-1067.

Samantaray, D., Chatterjee, C., Singh, R., Gupta, P. K., & Panigrahy, S. (2015). Flood risk modeling for optimal rice planning for delta region of Mahanadi river basin in India. *Natural Hazards*, 76(1), 347-372.

Sampson, C. C., Smith, A. M., Bates, P. D., Neal, J. C., Lorenzo, A., & Freer, J. E. (2015). A high - resolution global flood hazard model†. *Water Resources Research*, 51(9), 7358-7381.

Sanders, B. F. (2007). Evaluation of on-line DEMs for flood inundation modeling. *Advances in Water Resources*, 30(8), 1831-1843.

Schumann, G. J. P., Bates, P. D., Neal, J. C., & Andreadis, K. M. (2014). Technology: fight floods on a global scale. *Nature*, 507(7491), 169.

SCS, 1956. National Engineering Handbook, Hydrology, Section 4, Soil Conservation Service, US Department of Agriculture, Washington, DC.

Shi, H., Li, L., Eamus, D., Huete, A., Cleverly, J., & Tian, X., et al. (2017). Assessing the ability of MODIS EVI to estimate terrestrial ecosystem gross primary production of multiple land cover types. *Ecological Indicators*, 72, 153-164.

Shortridge, A., & Messina, J. (2011). Spatial structure and landscape associations of SRTM error. *Remote Sensing of Environment*, 115(6), 1576-1587.

Simard, M., Pinto, N., Fisher, J. B., & Baccini, A. (2011). Mapping forest canopy height globally with spaceborne lidar. *Journal of Geophysical Research: Biogeosciences*, 116(G4).

Soille, P. (2004). Optimal removal of spurious pits in grid digital elevation models. *Water Resources Research*, 40(12), 229-244.

Takaku, J., Iwasaki, A., & Tadono, T. (2016). Adaptive filter for improving quality of ALOS PRISM DSM. *Proceeding of IEEE Geoscience and Remote Sensing Symposium (IGARSS)*, 5370–5373.

Tarekegn, T. H., & Sayama, T. (2013). Correction of SRTM DEM artefacts by Fourier transform for flood inundation modeling. *Journal of Japan Society of Civil Engineers, Ser. B1 (Hydraulic Engineering)*, 69(4), I\_193-I\_198.

Varga, M., & Bašić, T. (2015). Accuracy validation and comparison of global digital elevation models over Croatia. *International Journal of Remote Sensing*, 36(1), 170-189.

Walker, W. S., Kelldorfer, J. M., & Pierce, L. E. (2007). Quality assessment of SRTM C- and X-band interferometric data: implications for the retrieval of vegetation canopy height.

*Remote Sensing of Environment*, 106(4), 428-448.

Wang, W., Yang, X., & Yao, T. (2012). Evaluation of ASTER GDEM and SRTM and their suitability in hydraulic Modeling of a glacial lake outburst flood in southeast Tibet. *Hydrological Processes*, 26(2), 213-225.

Ward, P. J., Renssen, H., Aerts, J. C. J. H., Van Balen, R. T., & Vandenberghe, J. (2008). Strong increases in flood frequency and discharge of the River Meuse over the late Holocene: impacts of long-term anthropogenic land use change and climate variability. *Hydrology and Earth System Sciences Discussions*, 12(1), 159-175.

Wilson, M., Bates, P., Alsdorf, D., Forsberg, B., Horritt, M., & Melack, J., et al. (2007). Modeling large - scale inundation of Amazonian seasonally flooded wetlands. *Geophysical Research Letters*, 34(15), 547-562.

Winsemius, H. C., Aerts, J. C. J. H., Beek, L. P. H. V., Bierkens, M. F. P., Bouwman, A., & Jongman, B., et al. (2015). Global drivers of future river flood risk. *Nature Climate Change*, 6(4).

Woodward, D., Hawkins, R., Hjelmfelt, A., Van Mullen, J., & Quan, Q., 2002. Curve Number method: origins, applications and limitations. Second Federal Interagency Hydrologic Modeling Conference, Las Vegas, Nevada

Xia, X., Liang, Q., Ming, X., & Hou, J. (2017). An efficient and stable hydrodynamic model with novel source term discretisation schemes for overland flow simulations. *Water Resources Research*.

Yamazaki, D., Baugh, C. A., Bates, P. D., Kanae, S., Alsdorf, D. E., & Oki, T. (2012). Adjustment of a spaceborne DEM for use in floodplain hydrodynamic modeling. *Journal of Hydrology*, 436, 81-91.

Yamazaki, D., Ikeshima, D., Tawatari, R., Yamaguchi, T., O'Loughlin, F., & Neal, J. C., et al. (2017). A high-accuracy map of global terrain elevations. *Geophysical Research Letters*, 44(11), 5844-5853.

Zandbergen, P. (2008). Applications of shuttle radar topography mission elevation data. *Geography Compass*, 2(5), 1404-1431.

Zhang, A., Zhang, C., Fu, G., Wang, B., Bao, Z., & Zheng, H. (2012). Assessments of impacts of climate change and human activities on runoff with SWAT for the Huifa River Basin, Northeast China. *Water resources management*, 26(8), 2199-2217.

Zhang, S., Wang, Z., Yan, B., Zhang, B., Song, K., & Liu, D. (2008). Relationship between landscape pattern and soil erosion of Huifa River Watershed. *Journal of Soil and Water Conservation*, 22(3), 29-35. (In Chinese)

## **Figure Captions**

**Fig. 1.** Hydraulic correction method for SRTM DEM in flood inundation modeling.

**Fig. 2.** The study area.

**Fig. 3.** The river networks of Huifa River Basin.

**Fig. 4.** DEM correction method to reconstruct flow connectivity.

**Fig. 5.** Example of DEM correction method to reconstruct flow connectivity.

**Fig. 6.** Comparing the simulated time series of water depth obtained on four different DEMs with measurements at 8 gauge stations.

**Fig. 7.** Comparing modeled water surface area with HJ imagery.

**Fig. 8.** Comparing simulated water depths in areas with vegetation response from the flood.



**Table 1. The root mean square errors (RMSE) and the difference of maximum (DI) of water depth variation**

| Number    | Station name | Contributing<br>area (km <sup>2</sup> ) | RMSE            |                       |                                |                                    | DI              |                       |                                |                                   |
|-----------|--------------|---|-----------------|-----------------------|--------------------------------|------------------------------------|-----------------|-----------------------|--------------------------------|-----------------------------------|
|           |              |   | Original<br>DEM | Bare-<br>Earth<br>DEM | Multi-Error-<br>Removed<br>DEM | Hydraulicall<br>y corrected<br>DEM | Original<br>DEM | Bare-<br>Earth<br>DEM | Multi-Error-<br>Removed<br>DEM | Hydraulically<br>corrected<br>DEM |
| Station 1 | Meihekou     | 1638                                    | 1.40            | 1.52                  | 1.25                           | 0.60                               | -3.16           | -3.51                 | -2.49                          | -0.84                             |
| Station 2 | Meihekoumei  | 442                                     | 1.14            | 1.21                  | 1.01                           | 0.51                               | -2.67           | -2.94                 | -2.72                          | -0.51                             |
| Station 3 | Dongfeng     | 481                                     | 1.59            | 1.59                  | 1.60                           | 1.39                               | -4.86           | -4.86                 | -4.86                          | -0.55                             |
| Station 4 | Liuhe        | 622                                     | 0.86            | 0.82                  | 0.74                           | 0.64                               | -3.14           | -3.01                 | -2.85                          | -1.42                             |
| Station 5 | Gushanzi     | 981                                     | 1.13            | 1.14                  | 1.10                           | 1.31                               | -2.23           | -2.53                 | -1.70                          | -0.21                             |
| Station 6 | Yangzishao   | 1957                                    | 1.44            | 1.44                  | 1.41                           | 2.28                               | -3.94           | -3.94                 | -3.94                          | 0.55                              |
| Station 7 | Panshixi     | 151                                     | 1.10            | 1.39                  | 0.84                           | 1.05                               | -1.56           | -0.83                 | -1.93                          | -2.39                             |
| Station 8 | Minli        | 1037                                    | 0.70            | 0.68                  | 0.54                           | 1.71                               | -0.14           | -0.50                 | 0.12                           | 2.51                              |

**Table 2. The overlap ratio between the model water surface area and HJ imagery observation**

| <b>River<br/>Number</b> | <b>Original DEM</b> | <b>Bare-Earth<br/>DEM</b> | <b>Multi-Error-<br/>Removed DEM</b> | <b>Hydraulically<br/>corrected DEM</b> |
|-------------------------|---------------------|---------------------------|-------------------------------------|--|
| 1                       | 0.67                | 0.65                      | 0.71                                | 0.79                                   |
| 2                       | 0.78                | 0.76                      | 0.76                                | 0.81                                   |
| 3                       | 0.87                | 0.87                      | 0.87                                | 0.87                                   |
| 4                       | 0.84                | 0.85                      | 0.83                                | 0.88                                   |
| 5                       | 0.55                | 0.55                      | 0.60                                | 0.73                                   |
| 6                       | 0.41                | 0.41                      | 0.56                                | 0.71                                   |
| 7                       | 0.78                | 0.77                      | 0.80                                | 0.85                                   |
| 8                       | 0.82                | 0.79                      | 0.83                                | 0.88                                   |
| 9                       | 0.70                | 0.65                      | 0.75                                | 0.81                                   |
| 10                      | 0.61                | 0.59                      | 0.62                                | 0.71                                   |
| 11                      | 0.37                | 0.37                      | 0.45                                | 0.63                                   |
| 12                      | 0.73                | 0.52                      | 0.71                                | 0.80                                   |

**Table 3. The percentage of predicted water depths in areas with vegetation response from flood**

| <b>Area</b>      | <b>DEM</b>              | <b>0 m</b> | <b>0 - 0.2 m</b> | <b>&gt; 0.2 m</b> |
|------------------|-------------------------|------------|------------------|-------------------|
| The whole basin  | Original                | 0.07       | 0.49             | 0.44              |
|                  | Bare-Earth              | 0.08       | 0.50             | 0.42              |
|                  | Multi-Error-Removed     | 0.05       | 0.41             | 0.55              |
|                  | Hydraulically corrected | 0.03       | 0.36             | 0.61              |
| Upstream basin   | Original                | 0.03       | 0.38             | 0.59              |
|                  | Bare-Earth              | 0.03       | 0.41             | 0.56              |
|                  | Multi-Error-Removed     | 0.02       | 0.36             | 0.62              |
|                  | Hydraulically corrected | 0.02       | 0.35             | 0.63              |
| Downstream basin | Original                | 0.11       | 0.60             | 0.29              |
|                  | Bare-Earth              | 0.13       | 0.61             | 0.26              |
|                  | Multi-Error-Removed     | 0.08       | 0.46             | 0.47              |
|                  | Hydraulically corrected | 0.05       | 0.36             | 0.59              |

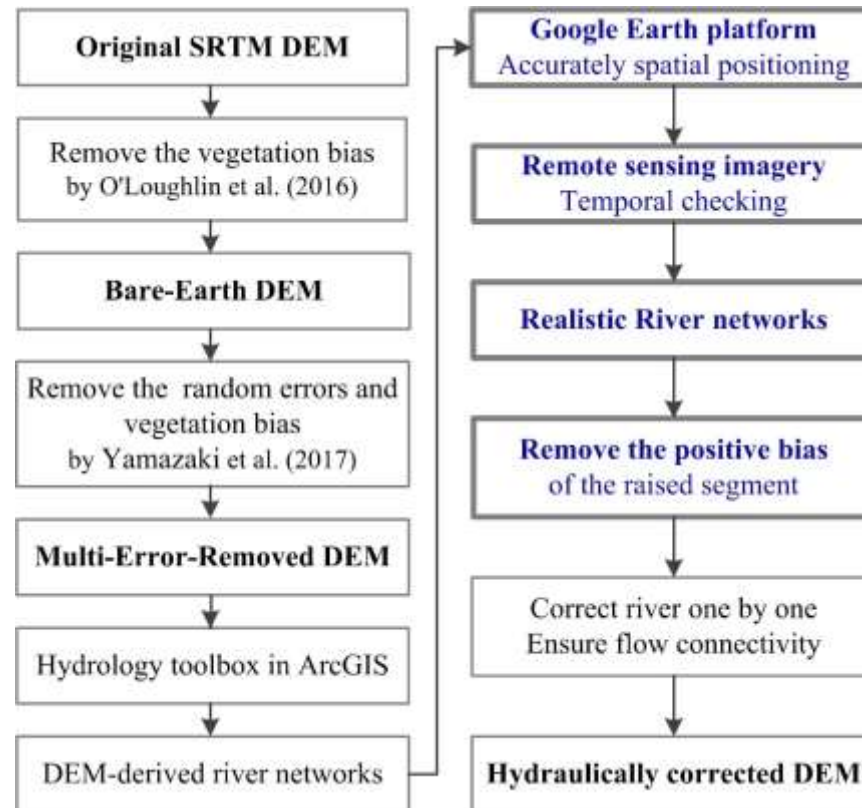
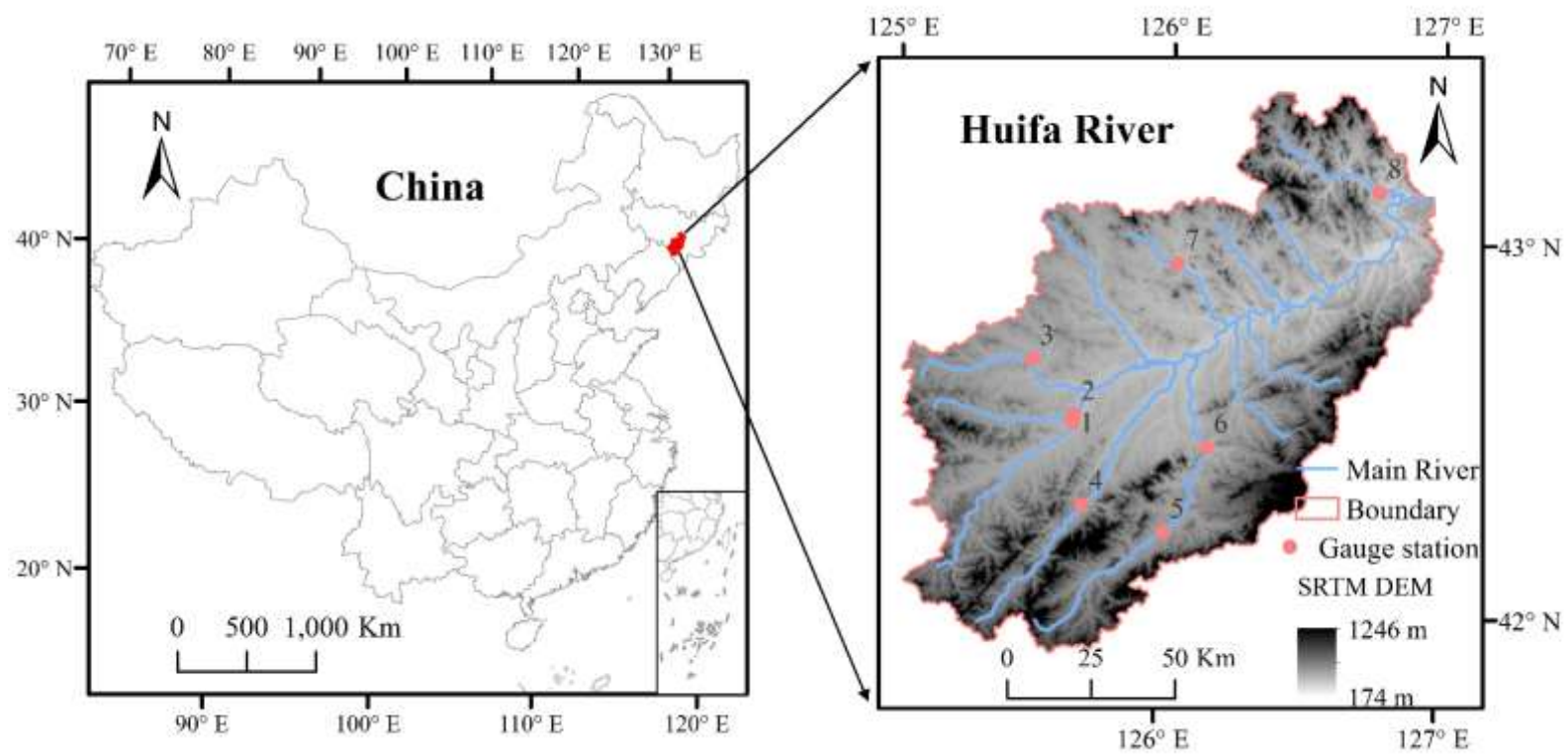
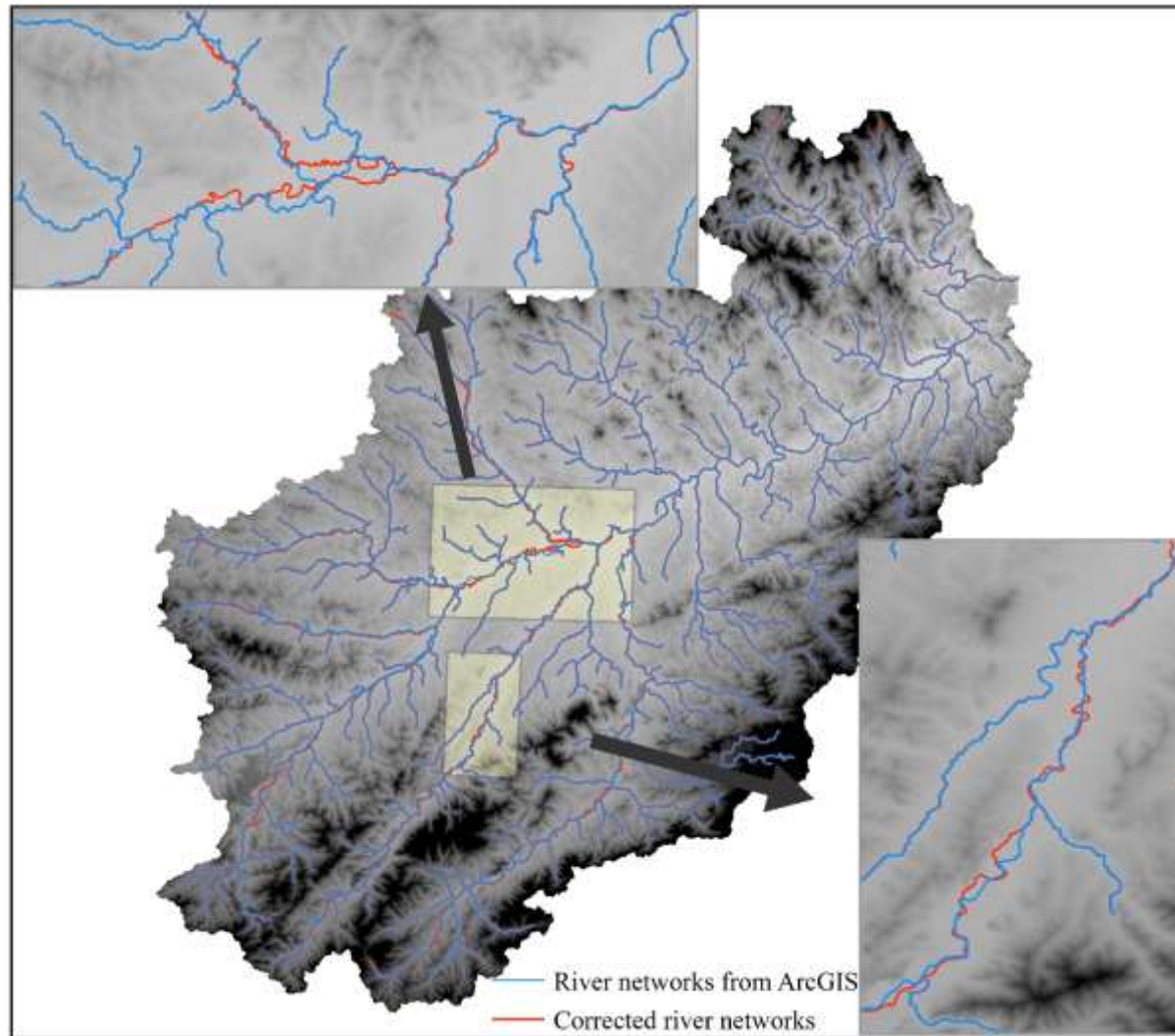


Fig. 1. Hydraulic correction method for SRTM DEM in flood inundation modeling



**Fig. 2. The study area**



**Fig. 3. The river networks of Huifa River Basin**





**Fig. 4. DEM correction method to reconstruct flow connectivity: (a) original elevation profile of main stream in Huifa River, (b) elevation value of segment 1 in (a), (c) elevation value of segment 2 in (a), (d) elevation value of segment 3 in (a), (e) elevation profile generation by DEM processing method**



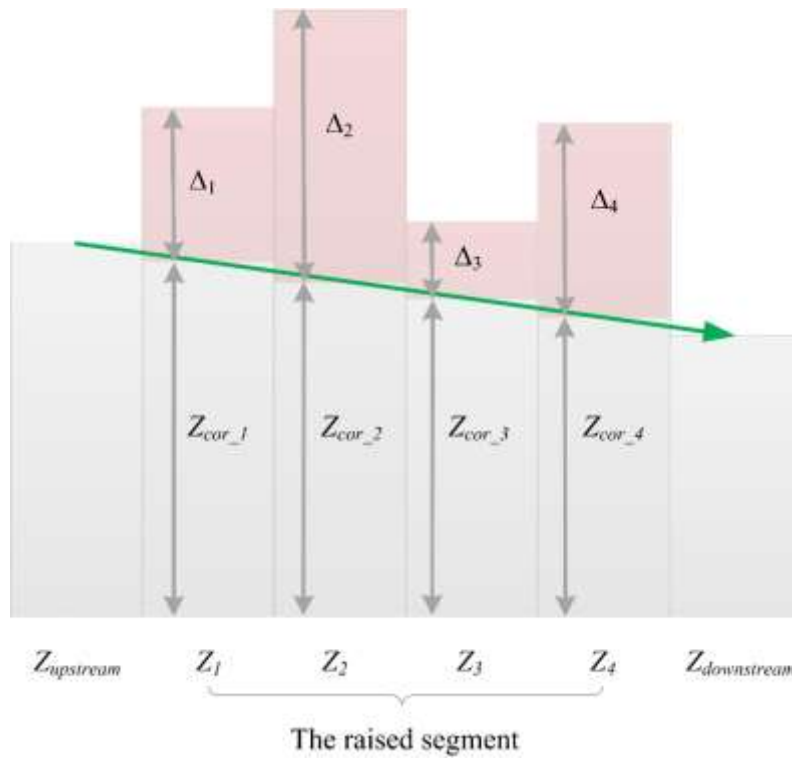


**Fig. 5. Example of DEM correction method to reconstruct flow connectivity.**

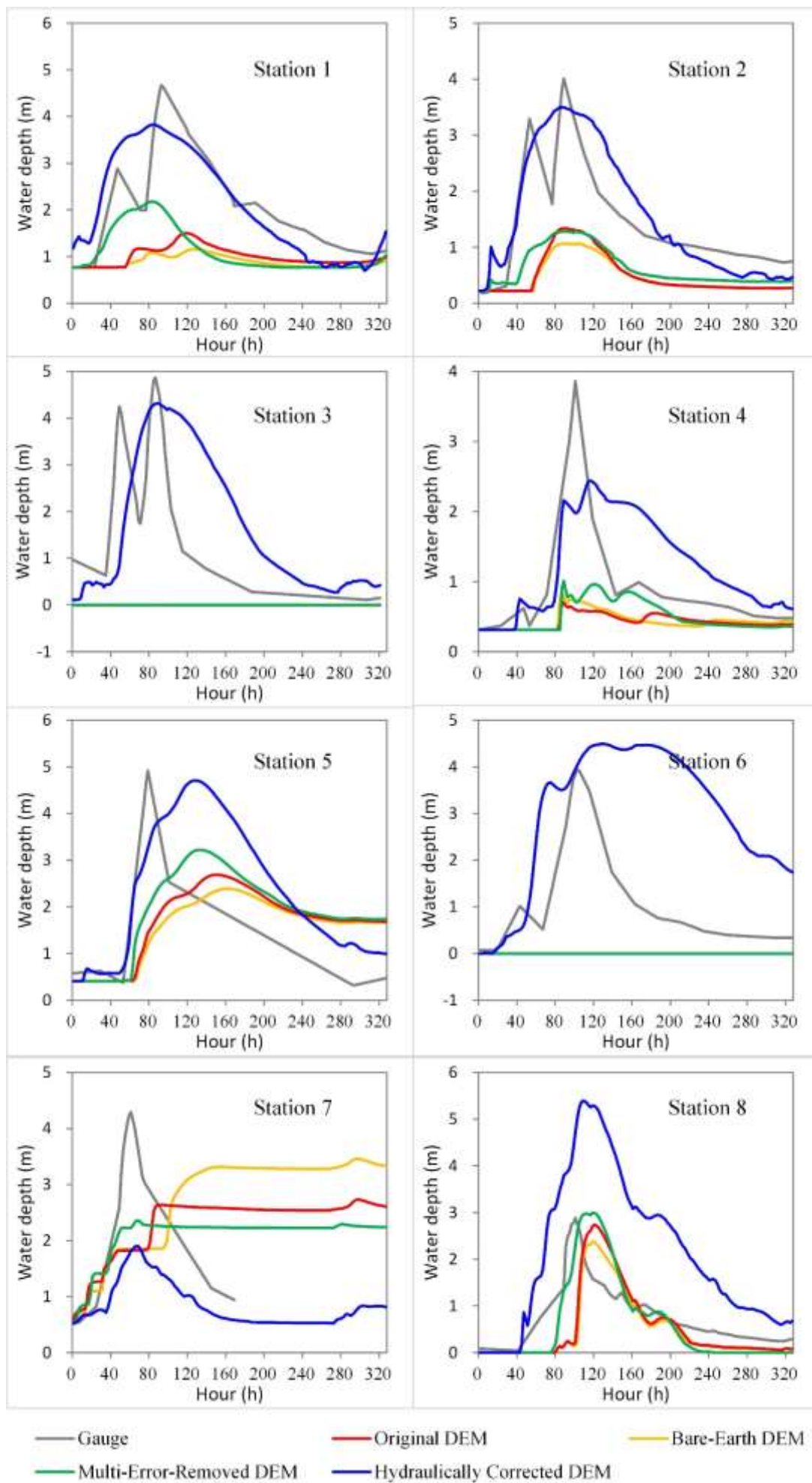


Fig. 6. Comparing the simulated time series of water depth obtained on four different DEMs with measurements at 8 gauge stations

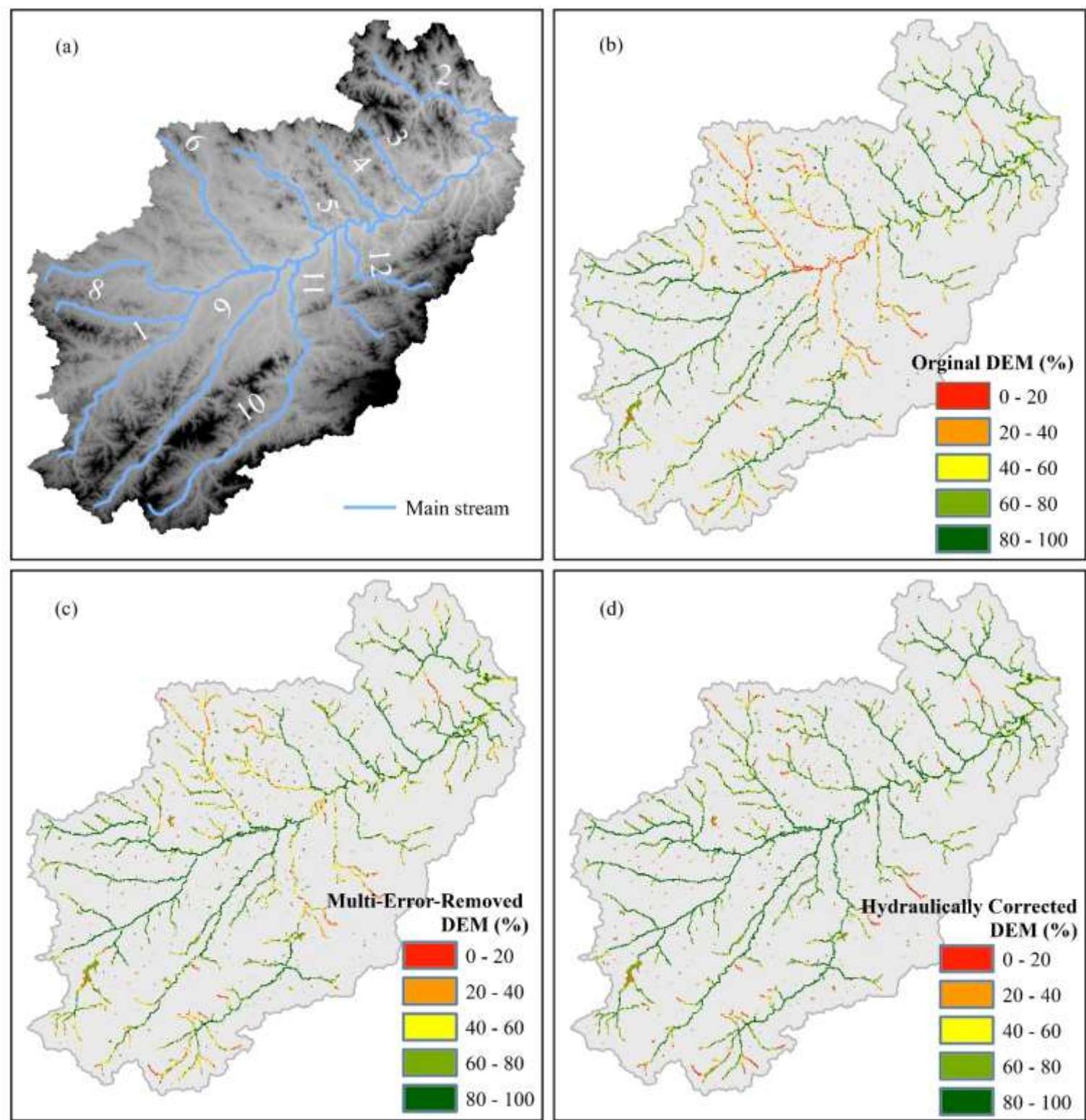
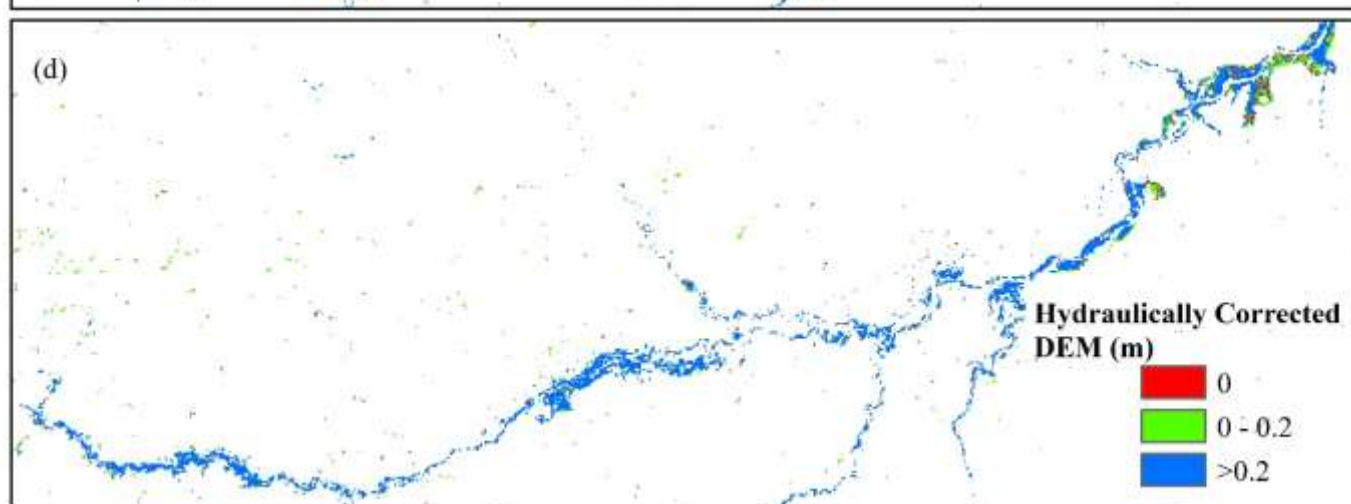
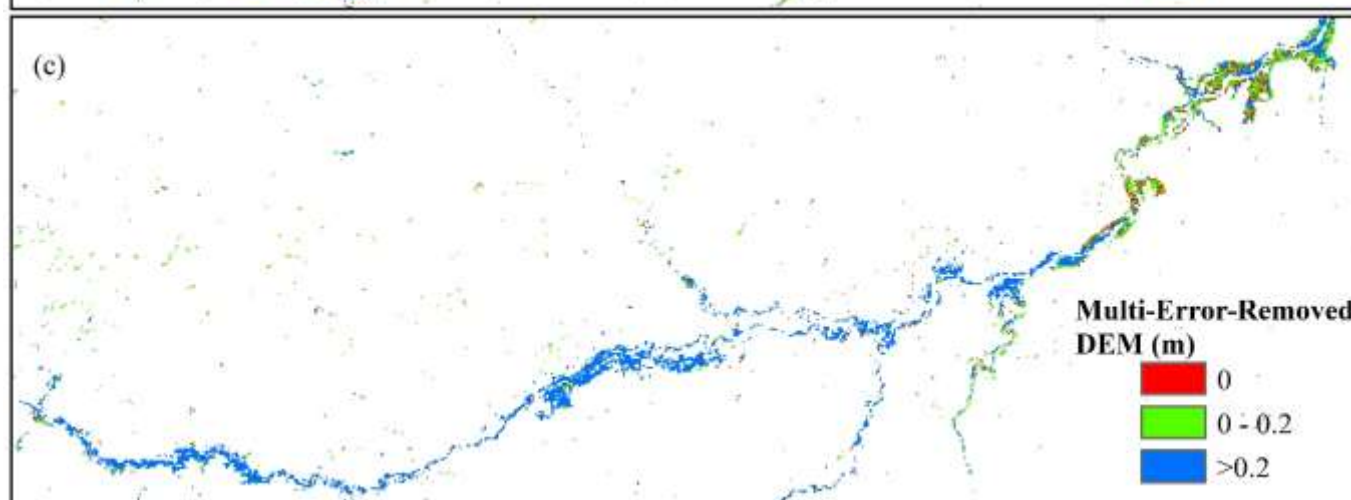
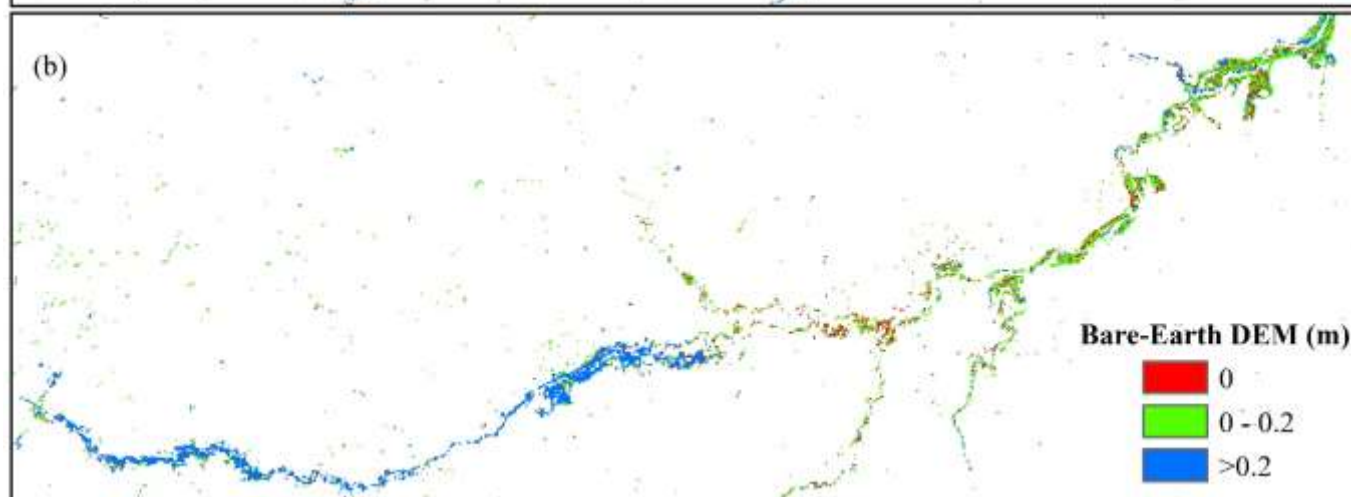
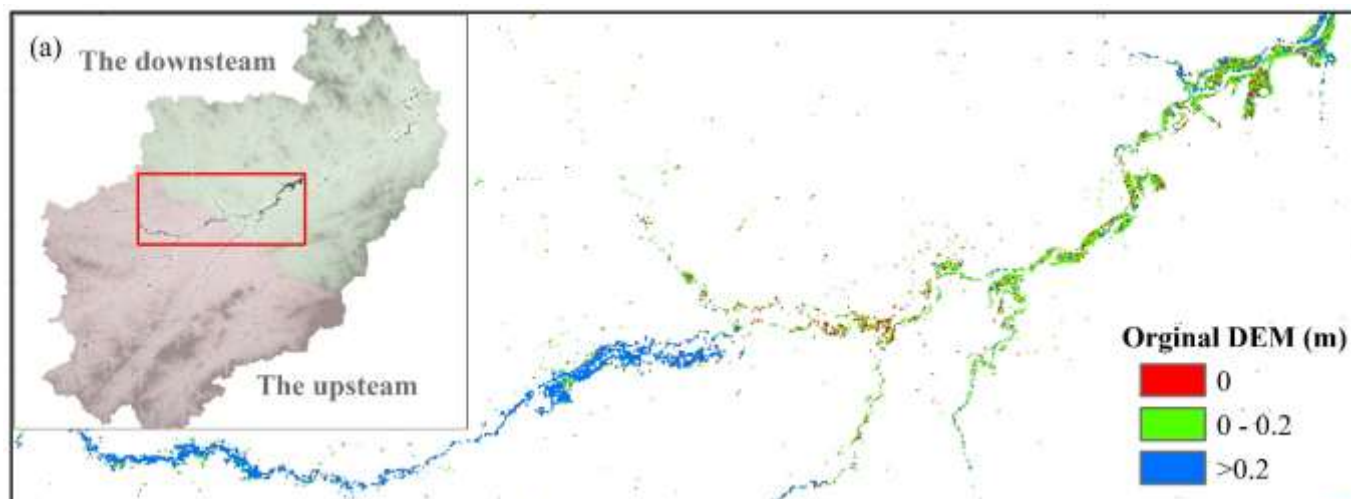


Fig. 7. Comparing modeled water surface area with HJ imagery (a) the main streams, (b) the overlap ratio of water surface with original DEM in 4\*4 pixels, (c) the overlap ratio of water surface with Bare-Earth DEM in 4\*4 pixels, (d) the overlap ratio of water surface with hydraulically corrected DEM in 4\*4 pixels





**Fig. 8. Comparing simulated water depths in areas with vegetation response from the flood under (a) original SRTM DEM, (b) bare-earth SRTM DEM, (c) Multi-Error-Removed DEM, (d) Hydraulically corrected DEM**